Discriminating power of milli-lensing observations for dark matter models

Nick Loudas

Supervisors: Prof. Vasiliki Pavlidou
Dr. Carolina Casadio

Department of Physics
University of Crete

This dissertation is submitted for the degree of
Master of Philosophy

Committee:
Prof. V. Pavlidou
Prof. J. Papadakis
Dr. C. Casadio

June 2023

To my loving family,
and Myrto

“... then one may improve the model by adding a head, ears, legs, color, and even a tail to the spherical cow."

Declaration

I hereby declare that except where specific reference is made to the work of others, the contents of this dissertation are original and have not been submitted in whole or in part for consideration for any other degree or qualification in this, or any other university. This dissertation is my own work and contains nothing which is the outcome of work done in collaboration with others, except as specified in the text and Acknowledgements. The information derived from the literature has been duly acknowledged in the text and a list of references provided.

Nick Loudas
June 2023

Acknowledgements

I would like to express my deepest gratitude to my supervisors Prof. Vasiliki Pavlidou and Dr. Carolina Casadio for their continuous support and guidance throughout this year, and for helping me choose such an interesting and challenging topic in cosmology. Their expertise and constructive feedback significantly shaped the direction of my research, and helped me overcome several challenges and achieve meaningful results. I am deeply indebted to Prof. Kostas Tassis for his invaluable contribution to this thesis and for his insightful comments. I would also like to extend my sincere thanks to Prof. Joe Silk, Prof. Hai-bo Yu, and Dr. Daniel Gilman for their valuable feedback that helped me improve this thesis and for the fruitful discussions on the science case. Many thanks to the members of the SMILE group whose contribution was seminal. I would like to thank all faculty members and staff of the University of Crete and the Institute of Astrophysics-FORTH for maintaining a stimulating environment and for providing me the opportunity to interact with prominent scientists and attend high-level colloquia and seminars. Special thanks should go to my officemates, A. Tsouros, E. Kyritsis, D. Alvarez-Ortega, C. Lofaro, A. Konstantinou, A. Kumar, and all graduate students at the IAFORTH for creating a vibrant and collaborative work environment for one to work and have pleasant breaks at the same time. My deepest appreciation to M. Falalaki, whose unwavering support, encouragement, and understanding have been invaluable throughout this journey.

Lastly, I could not have undertaken this journey without the continuous guidance from my mentor, Prof. Nick Kylafis, who has been an endless source of inspiration throughout all my first academic steps into research.

This thesis has received funding from the European Research Council (ERC) under the HORIZON ERC Grants 2021 program under grant agreement No. 101040021.

Abstract

The nature of dark matter (DM) is still under intense debate. Subgalactic scales are particularly critical, as different, currently viable DM models make diverse predictions on the expected abundance and density profile of DM haloes on these scales. In this thesis, we investigate the ability of subgalactic DM haloes to act as strong lenses on background compact sources, producing gravitational lensing events on milli-arcsecond scales (milli-lenses), for different DM models. For each DM scenario, we explore whether a sample of ~ 5000 distant sources is sufficient to detect at least one milli-lens.

We developed a semi-analytical model to estimate the milli-lensing optical depth as a function of the source's redshift for various DM models. We employed the Press-Schechter formalism, as well as results from recent N-body simulations to compute the halo mass function, taking into account the appropriate spherically averaged density profile of haloes for each DM model. We treated the lensing system as a point-mass lens and invoked the effective surface mass density threshold to calculate the fraction of a halo that acts as a gravitational lens. We studied three classes of dark matter models: cold DM, warm DM, and self-interacting DM.

We find that haloes consisting of warm DM turn out to be optically thin for strong gravitational milli-lensing (zero expected lensing events). Cold DM haloes may produce lensing events depending on the steepness of the concentration-mass relation. Self-interacting DM haloes can efficiently act as gravitational milli-lenses only if haloes experience gravothermal collapse, resulting in highly dense central cores. The redshift distribution of the source sample is fundamental in estimating the expectation number of detected milli-lenses under a specified DM scenario.

Table of contents

List of figures

Chapter 1

Introduction

One of the most groundbreaking findings during the last century was the discovery of a mass excess in nearby galaxies that could not be explained by the amount of ordinary (luminous) matter that was found to exist in those galactic systems. The observation of flat rotation curves in spiral galaxies (e.g., Bosma, 1981; Corbelli and Salucci, 2000; Rubin et al., 1980), the discrepancy between observed velocity dispersion measurements and those predicted by the virial theorem in elliptical galaxies and globular clusters (e.g., Faber and Jackson, 1976; Zwicky, 1933), and the presence of collapsed structures at high redshift (e.g., Gunn and Gott, 1972) were incontrovertible evidence for the existence of a new extraordinary form of matter in the Universe, called dark matter (DM), which neither emits nor absorbs radiation. The DM hypothesis has led to several correct predictions and has explained many observational discrepancies that had emerged in the past from the comparison of observational data with the first cosmological scenarios that were dust-radiation-only models. Despite the great success of the DM model, its nature remains unknown, making it one of the most fundamental unsolved questions in physics.

1.1 Dark matter

1.1.1 ΛCDM successes & challenges

The most widely accepted scenario for the origin of DM is the so-called cold dark matter (CDM), a part of the standard ΛCDM cosmological model, that has been remarkably successful in explaining the properties of a wide range of large-scale observations, including the accelerating expansion of the Universe (Perlmutter et al., 1999), the power spectrum of the cosmic microwave background (CMB) (Page et al., 2003), and the observed abundances of different types of light nuclei (Cyburt et al., 2016). However, the ΛCDM paradigm still

presents some discrepancies with observations, mostly at small scales. Such small-scale challenges include, among others, the "cusp-core" problem, the missing satellites problem, the too-big-to-fail problem, and the angular momentum catastrophe (for a review, see Bullock and Boylan-Kolchin 2017; see also Perivolaropoulos and Skara 2022). An appealing solution to those problems is to modify the intrinsic properties of DM particles.

1.1.2 DM alternatives

During the past few years, numerous DM alternatives and ΛCDM extensions have been proposed by several authors, with the purpose to address some of the ΛCDM challenges. One of the most promising DM alternatives is the warm dark matter (WDM) model (e.g., Lovell et al., 2012; Viel et al., 2005), where particles have a rest mass on the order of a few keV, such as sterile neutrinos or thermal relics, that had non-negligible velocities at early times. Another very popular DM scenario is the self-interacting dark matter (SIDM) model where particles interact with each other (e.g., Spergel and Steinhardt, 2000) having non-negligible cross sections, on the order of $\sim 1\,\mathrm{cm}^2/\mathrm{g}$ (e.g., Zavala et al., 2013). Other more exotic DM alternative particle-physics theories include the following: ultra-light axion dark matter (Schwabe et al., 2016), dark atoms (for a review, see Cline, 2021), and fuzzy dark matter (e.g., Kulkarni and Ostriker, 2022). Although these latter models are not examined here, the toolkit we have developed can be straightforwardly adapted to any DM model for which the redshift-dependent mass function and the density profile of haloes and subhaloes can be calculated.

The properties of the DM particle affect the formation of DM structures on all scales, their stability, as well as their evolution in time. In addition, the fundamental attributes of DM particles modify the primordial power spectrum describing the initial overdensity seeds of cosmological structures. So, differences in the intrinsic DM particle properties between different models are expected to lead to measurable deviations in the resulting mass function of collapsed objects. For instance, models that include light particles (i.e., with very low mass), such as WDM, feature a sharp cutoff in the differential halo mass function below a critical mass scale, which is closely related to the rest mass of the DM particle. The mildly relativistic velocities of WDM particles in the early Universe were high enough to wash out almost any small-scale density fluctuations (free streaming) emerged in the primordial power spectrum below a specific length scale, called free-streaming length, thereby leading to the suppression of structures below sub-galactic scales (e.g., Melott and Schramm, 1985; Viel et al., 2005).Moreover, the density profile (i.e., internal mass distribution) of DM haloes also turns out to be noticeably different from model to model. For example, virialized haloes

made of WDM particles typically have lower central densities with respect to CDM haloes of the same mass, by virtue of their generally later formation epochs (e.g., Lovell et al., 2012).

The study of DM haloes below subgalactic scales turns out to be particularly crucial for the exploration of the nature of DM. Nevertheless, it is extremely challenging to detect such haloes directly, in order to either measure their number density in the Universe or examine their internal structure, since they might not even form galaxies due to their small size. So, the only possible way to explore and study them is through gravitational effects.

1.2 Strong gravitational lensing

1.2.1 Theory

One of the most promising methods of detecting subgalactic DM haloes is strong gravitational lensing, where light that passes near a massive object (the lens) is being deflected, traveling a longer path than it would in the absence of the gravitational potential of the lens (e.g., Weinberg, 1972). As a result, when a compact background source (for instance, a radio loud quasar) emits radiation with the lens being in between the source and the observer and close enough to the line of sight, then the path of the light is affected strongly, resulting in the emergence of multiple images of the background source on sky with different magnifications (e.g., Vegetti et al., 2012), provided its projected surface density exceeds a threshold. This effect is commonly known as strong lensing (see for example, Wright and Brainerd, 2000). In the special case where the source displays intrinsic variability, observable time delays between the different images (pulses) may occur (Zackrisson and Riehm, 2010).

1.2.2 Previous studies

Gravitational lensing can be used to detect compact objects (COs) that could not be detected otherwise, such as primordial black holes (PBHs) or dense DM haloes. Press and Gunn (1973) introduced the idea of assessing the cosmological abundance of COs through their strong gravitational lensing effect on distant background sources. They demonstrated that the cosmological mass density of COs can be constrained by deriving the fraction of lensed radio sources. Later on, Wilkinson et al. (2001) carried out a search for milli-lenses (gravitational-lensing images with milli-arcsec separations) in Very Long Baseline Interferometry (VLBI) observations of a sample of 300 compact radio sources, but no lensed systems in the mass range $\sim 10^6\,\mathrm{M}_\odot$ to $\sim 10^8\,\mathrm{M}_\odot$ were found. Their negative result allowed them to place an upper limit $\Omega_{\mathrm{CO}} \lesssim 0.01$ (95% confidence) on the cosmological density of COs in this mass range, concluding that the contribution of a primordial supermassive BHs population to

the dark matter content of the Universe is negligible. The currently ongoing Search for MIlli-LEnses (SMILE) project (Casadio et al., 2021) expands the search for milli-lenses (i.e, lens systems that produce lensed images of a background compact source with angular separation on the order of milli-arcseconds) in the lens mass range $\sim 10^6\,\mathrm{M}_\odot$ to $\sim 10^9\,\mathrm{M}_\odot$, to a large and complete sample of ~ 5000 radio-loud sources using VLBI data.

1.3 Purpose of this study

Motivated by the potential of the SMILE project, in this work we develop a novel method to exploit its upcoming results (i.e., the fraction of lensed quasars) with the purpose to derive constraints on the nature of DM and discriminate between currently viable DM scenarios. Our approach is based on the concept of the lensing optical depth, representing the probability for an observed source to be gravitationally lensed by a foreground mass distribution. The prescription for the implementation of this method can be found in Zackrisson and Riehm (2007). Recently, several authors have followed similar approaches to place limits on the abundance of PBHs, using Fast Radio Bursts (FRBs) (e.g., Leung et al., 2022; Zhou et al., 2022a,b), Gamma-ray Bursts (GRBs) (e.g., Kalantari et al., 2021), afterglows of GRBs (Gao et al., 2022), and compact radio sources (Zhou et al., 2022c), while others explore the diffractive lensing of gravitational waves (GWs) emanating from binary black hole mergers by small DM haloes to probe the nature of DM (see Guo and Lu, 2022).

Here, we pursue the possibility of subgalactic DM haloes acting as gravitational milli-lenses. The mass scales that we focus on are of great importance, since they might provide a unique opportunity to advance our knowledge concerning the properties of DM particles and rule out some DM scenarios for two fundamental reasons: 1) they coincide with the mass scale below which significant deviations between mass functions and density profiles of various DM models start to emerge (see for example, Bose et al., 2016, and our Sect. 3) which eventually result in different expectation numbers of lensing events; 2) the contribution of baryonic matter in cosmological sub-galactic DM haloes is almost negligible (in particular haloes with mass below $\sim 3\times 10^8\,\mathrm{M}_\odot$ are not expected to form galaxies; see Benitez-Llambay and Frenk, 2020).

We derive the expected number of milli-lenses in the source sample of the SMILE project for various DM models by calculating the milli-lensing optical depth as a function of the source's redshift. This in turn depends on the halo mass function, as well as on the projected surface mass density. Both of these physical quantities have noticeable differences between various scenarios, and hence the milli-lensing optical depth exhibits differences between DM models.

The layout of this thesis is as follows. In Sect. 2 we describe our calculation of the milli-lensing optical depth. In Sect. 3 we discuss the analytic descriptions we use for the structure of DM haloes for various cosmological DM scenarios, and their corresponding mass functions. In Sect. 4 we present the results of our calculations, which we discuss in Sect. 5

Chapter 2

Lensing probabilities

The principal result of any survey for lensing systems in the observable Universe is the number of confirmed lensed images in a complete sample of sources (e.g., Browne et al., 2003; Myers et al., 2003). Such a result, immediately reveals the statistical density of gravitational lens candidates within the cosmological space determined by the cosmological location of the observatory and the position of the most distant source included in the source sample. This number, however, cannot directly yield important constraints related to the abundance of DM haloes in the Universe, i.e. the mass function, and/or the profile of lens' mass distribution. To maximize the constraining power of this product, we have to connect it to theoretical models that predict the expectation value of lensing events taking into account the differences in the abundance and density profile of DM haloes between various DM models. In such a way, the observational result can be compared directly with the theoretically predicted ones, leading to viable inferences regarding the properties or/and shape of gravitational lens systems composed of DM. So, a rigorous method that connects theory with observations is required for solid conclusions to be deduced.

The most straightforward way to achieve this is to compute the lensing optical depth for any given DM scenario. Subsequently, the amount of observed lensed objects detected in a given sample can be linked to theory and provide stringent constraints on the nature of DM by investigating what properties of DM particles produce such a lensing optical depth that leads to an expectation value of lensing events which matches with the observed one.

The lensing optical depth depends strongly on the mass function of gravitational lenses and on the surface density profile of each halo, which essentially is related to the density profile. It also depends on the cosmology. In this paper, we fix the cosmological parameters to be $H_0 = 100\ h$ km s^{-1} Mpc^{-1}, $h = 0.7$, $\Omega_m = 0.3$, $\Omega_\Lambda = 0.7$, $n = 0.97$, $\delta_c(0) = 1.674$, and $\sigma_8 = 0.8$. The overall results, however, are not sensitive to small variations in these parameters. It is out of our scope to investigate the behavior of lensing optical depth

for different cosmological models, and hence we adopt the widely accepted concordance cosmology, where $\Omega_m + \Omega_\Lambda = 1$.

2.1 Milli-lensing optical depth

In order for our results to be applicable to the SMILE project, we are interested in lenses that produce multiple images with angular separation on the order of milli-arcseconds (milli-lenses). Thus, we focus on lenses of masses $(10^6 - 10^9)\,\mathrm{M}_\odot$, which result in lensed images of angular separation that lie on the range $\sim (3-100)$ mas, considering both the lens and the source to be at cosmological distances. For the calculation of the milli-lensing optical depth, we adopt the prescription of Zackrisson and Riehm (2007), which makes use of the point-mass lens model. We treat the lens as a massive object of mass M_l with an angular Einstein radius

$$\beta_E = \sqrt{4\frac{GM_l}{c^2}\frac{D_{ls}}{D_{ol}D_{os}}}, \tag{2.1}$$

where D_{os}, D_{ls}, and D_{ol} are the angular-diameter distances from the observer to the source, from the lens to the source, and from the observer to lens, respectively, with the lens being at redshift z while the source is located at redshift z_s. The angular-diameter distance D_{AB} from a point A to B is obtained though the Friedman-Robertson-Walker metric

$$\mathrm{d}s^2 = (c\mathrm{d}t)^2 - a^2(t)\left[\mathrm{d}r^2 + r^2\mathrm{d}\Omega^2\right],$$

and is given by

$$D_{AB}(t_A, t_B) = a(t_B)\int_{t_A}^{t_B}\frac{cdt}{a(t)}, \tag{2.2}$$

where $a(t)$ is the scale factor.

D_{AB} can be also written as

$$D_{AB}(z_A, z_B) = \frac{c}{1+z_B}\int_{z_A}^{z_B}\frac{dz}{H(z)}, \tag{2.3}$$

where $H(z)$ is the Hubble parameter. Using Friedmann cosmological equations that are solutions of Einstein's field equations for a spatially flat, isotropic, and homogeneous Universe, we obtain the dependence of the Hubble's parameter, H(z) on the redshift, z, namely

$$\left(\frac{H(z)}{H_0}\right)^2 = \Omega_m(1+z)^3 + \Omega_\Lambda, \tag{2.4}$$

with Ω_m, Ω_Λ referring to the present values of the density parameters for matter and dark energy, respectively. We note that, the redshift is a function of time and its dependence on time is described by the following useful formula

$$c\frac{dt}{dz} = -\frac{c}{H_0}\frac{1}{(1+z)\sqrt{\Omega_m(1+z)^3+\Omega_\Lambda}} \tag{2.5}$$

The milli-lensing optical depth for a source at redshift z_s is given by

$$\tau(z_s) = \int_0^{z_s}\left|\frac{cdt}{dz}\right| dz \int_{10^6\mathrm{M}_\odot}^{10^9\mathrm{M}_\odot} \sigma(M_l,z,z_s)\frac{dn(M_l,z,z_s)}{dM_l}dM_l, \tag{2.6}$$

where $\sigma(M_l,z,z_s)$ is the lensing (effective) cross section

$$\sigma(M_l,z,z_s) \equiv \pi\beta_E^2 D_{ol}^2 = \frac{4\pi G M_l}{c^2}\frac{D_{ol}D_{ls}}{D_{os}}, \tag{2.7}$$

and dn/dM_l is the differential lens mass function

$$\frac{dn(M_l,z,z_s)}{dM_l} = \frac{dM(M_l,z,z_s)}{dM_l}\frac{dn(M,z)}{dM}. \tag{2.8}$$

In Eq. (2.8), dn/dM is the differential halo mass function (see §3.2). We caution the reader of the two different masses entering Eq. (2.8): the lens mass M_l, and the halo mass M. These two are not in general the same because only the part of the halo in which the projected surface mass density exceeds the critical strong lensing threshold can act as a gravitational lens. The critical surface density value for a source at redshift z_s undergoing strong gravitational lensing by a foreground DM halo (lens) at redshift z is

$$\Sigma_{cr}(z,z_s) \equiv \frac{M_l}{\sigma(M_l,z,z_s)} = \frac{c^2}{4\pi G}\frac{D_{os}}{D_{ol}D_{ls}} \gtrsim 10^9\,\mathrm{M}_\odot\,\mathrm{kpc}^{-2}. \tag{2.9}$$

In Fig. 2.1, we show a heat map of the critical surface density value (effective threshold) as a function of the source redshift z_s and lens redshift z_l. The values of the effective threshold for strong lensing are extremely sensitive to the relative positions of the lens, source and observer. When the lens angular-diameter distance from the observer is comparable to the distance between the lens and the source (i.e., $D_{ol} \sim D_{ls}$), then the effective threshold tends to get lower values with respect to the case where the lens is either pretty close to the observer (i.e., $z_l \gtrsim 0$) or the source (i.e., $z_l \lesssim 0$), respectively. In the latter case, the effective threshold value becomes remarkably higher than the minimum one.

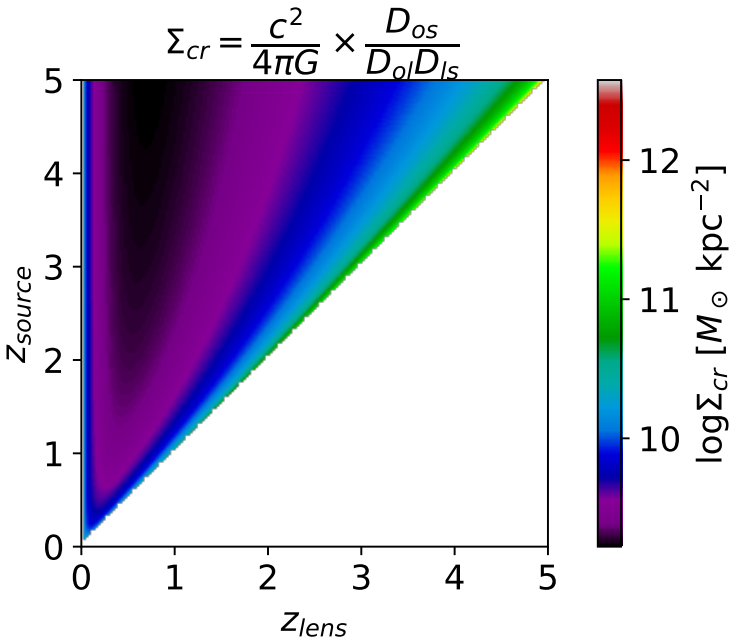

Fig. 2.1 Critical surface density value (effective threshold for strong lensing) as a function of the source and lens redshifts. The critical surface density function is given in Eq. (2.9).

In order to calculate the halo mass M for given M_l, z, and z_s, we demand a solution of the equation

$$\Sigma(M; M_l, z) = \Sigma_{cr}(z, z_s), \tag{2.10}$$

where Σ is the projected halo surface density described extensively in Sect. 3. Solving this equation numerically, we obtain $M(M_l, z, z_s)$. We use the central finite difference approximation to estimate the derivative dM/dM_l, which appears in Eq. (2.8). Given that the halo surface mass density is obtained after an integration of the density profile, it is clear that the results will differ significantly from model to model, since each DM scenario predicts a different density profile.

2.2 Expectation value of lensing events

Once we obtain the milli-lensing optical depth, we evaluate the expectation number of lensing events in the SMILE source sample using

$$N_l = \sum_{i=1}^{N_{sources}} 1 - \exp\left(-\tau(z_{s,i})\right). \tag{2.11}$$

For $\tau \ll 1$, we can approximate Eq. (2.11) by

$$N_l \approx \sum_{i=1}^{N_{sources}} \tau(z_{s,i}). \tag{2.12}$$

The source sample, as well as their corresponding redshifts are described next.

2.3 SMILE sample

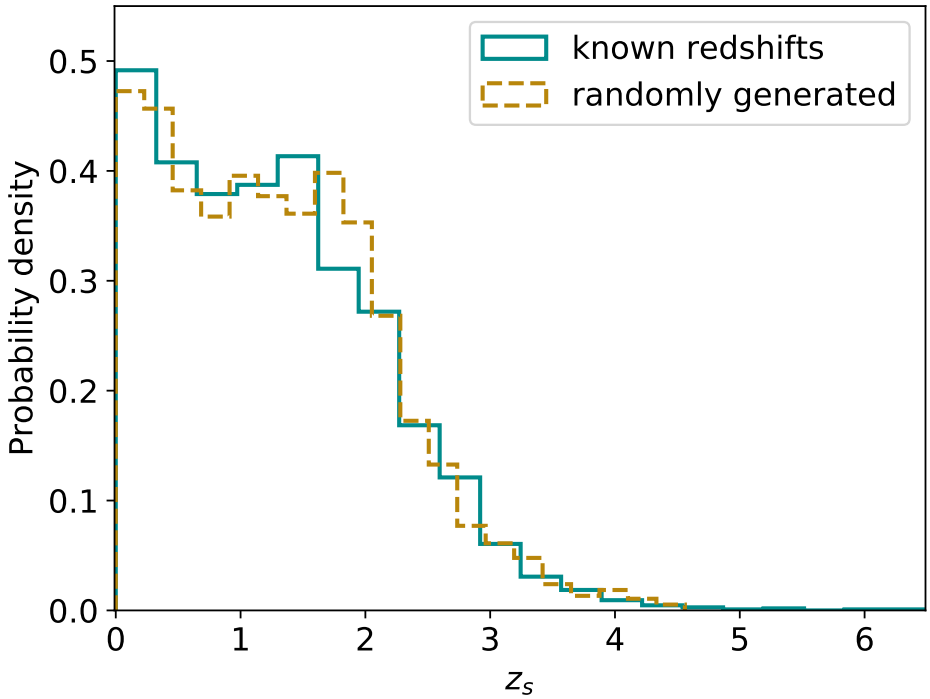

Fig. 2.2 Redshift distribution for sources used in this study. Cyan solid line represents the redshift distribution of sources with known redshift, whereas golden dashed line stands for the distribution of the randomly selected redshift measurements from the known redshift sample.

The source sample considered in this study is the one of SMILE[1]: a complete sample built starting from the complete sample used in the Cosmic Lens All-Sky Survey (CLASS; Browne et al., 2003; Myers et al., 2003), the most successful search to date for gravitational lens systems at galactic scales using radio frequencies. The complete sample of 11685 sources

[1] https://smilescience.info/

presented in CLASS is drawn from two other catalogs: the 5 GHz GB6 catalog (Gregory et al., 1996), and the 1.4 GHz NVSS catalog (Condon et al., 1998). The CLASS catalog contains sources from declination 0° to 75°, with a minimum flux density of 30 mJy at 5 GHz, flat spectral index (< 0.5) between 1.4 and 5 GHz, and Galactic latitude ($|b| \geq 10°$). The complete sample of 11685 sources has been initially followed up in CLASS with low resolution Very Long Array (VLA) observations at 8 GHz. The SMILE started from the complete sample in CLASS and selected sources with total flux density at 8 GHz $\geq$ 50 mJy. The 4968 sources that satisfy such a requirement make a complete sample of flat spectrum sources at declination [0°, +75°].

In order to obtain redshift measurements for sources in the SMILE sample, we used the Optical Characteristics of Astrometric Radio Sources (OCARS) catalog (Malkin, 2018), containing redshift measurements of a large number of radio sources observed in different VLBI astrometry programs. Of the 4968 sources in SMILE, 2781 have an optical counterpart within 3 arcsec with redshift measurements in OCARS. For the remaining sources we searched for an optical counterpart within 3 arc seconds, with known redshift, in NED[2]. In total, we collected redshifts for $\sim 2/3$ of sources in SMILE. For the remaining $\sim 1/3$, we followed a rather conservative approach generating redshift measurements by randomly selecting values from the known redshift sample. Their distribution is shown in Fig. 2.2.

[2]The NASA/IPAC Extragalactic Database (NED) is funded by the National Aeronautics and Space Administration and operated by the California Institute of Technology.

Chapter 3

DM haloes & mass functions

3.1 Halo size & structure

The internal structure of dark matter haloes affects the lensing optical depth, since the threshold for strong gravitational lensing is associated with the projected surface mass density, which in turn is related to the shape of the density profile. For a detailed review of the various mass densities see Zavala and Frenk (2019), while a thorough comparison among various density profiles can be found in Merritt et al. (2006) work.

An important finding of the past decades is that spherically averaged DM density profiles in N-body cosmological simulations have a universal form (Navarro et al., 1997). Such density profiles are described by a simple functional form characterized by only two free parameters. The first one is the concentration parameter, denoted by c_Δ, which quantifies how concentrated the mass is toward the center of the halo. The other one is the characteristic radius, r_s, which determines the distance from the center above which the density profile becomes steeper, that is to say quantifies roughly the size of the core. These two parameters are related to each other through

$$c_\Delta = \frac{r_\Delta}{r_s}, \tag{3.1}$$

where r_Δ is the virial radius.

Since the distribution of mass is continuous, the boundary of a halo cannot be defined precisely. So, another major challenge is to come up with a robust method of determining the size of a halo uniquely. Thus far, numerous papers that deal with this problem have been published by several authors (Cole and Lacey, 1996; Cuesta et al., 2008; White, 2001; Zavala and Frenk, 2019). In general, the radius of a halo can be defined through the overdensity parameter, $\Delta(z)$, which in principle depends on the cosmology (Bryan and Norman, 1998; Naderi et al., 2015; Seppi et al., 2021; Tinker et al., 2008). In particular, it represents the

radius where the mean interior density is $\Delta(z)$ times the critical density of the Universe $\rho_{cr}(z)$, namely

$$\frac{3}{4\pi r_{\Delta}^{3}}\int_{0}^{r_{\Delta}}\rho(\vec{r})d^{3}\vec{r}=\Delta\rho_{cr}, \tag{3.2}$$

where the critical density is given by

$$\rho_{cr}(z)=\frac{3H^{2}(z)}{8\pi G}=\rho_{cr,0}\left(\frac{H(z)}{H_{0}}\right)^{2}, \tag{3.3}$$

with G being the Newtonian gravitational constant, while $\rho_{cr,0}$ accounts for the critical density of the Universe at redshift $z=0$, and $H(z)$ is given in Eq. (2.4).

The halo mass M_{Δ}, which is the mass contained within a sphere of radius r_{Δ}, is given by

$$M_{\Delta}=\Delta\frac{4\pi}{3}r_{\Delta}^{3}\rho_{cr}, \tag{3.4}$$

and as a result the halo radius can also be written as

$$r_{\Delta}(M_{\Delta},z)=\left(\frac{3M_{\Delta}}{4\pi\Delta\rho_{cr}(z)}\right)^{1/3}. \tag{3.5}$$

However, the most commonly used way to determine the halo's size is to consider that the overdensity parameter Δ is fixed and equal to 200, since it turns out to be a rather convenient way to define the boundary of the halo and simplifies the calculations (e.g., Cole and Lacey, 1996). Taking this fact into account, we fix the overdensity to be $\Delta=200$, throughout this paper, and therefore the halo mass is M_{200} (hereafter, M), the halo radius is r_{200}, and the concentration is c_{200} (hereafter, c).

Other quantities used extensively below are the enclosed mass, M_{enc}, the projected surface mass density, Σ, and the lens mass, M_{l}. The enclosed mass is defined as the mass that is contained within a sphere of radius r, namely

$$M_{enc}(r)=4\pi\int_{0}^{r}r'^{2}\rho(r')\,dr', \tag{3.6}$$

where we assume that we deal with spherically symmetric objects. The projected surface density is derived simply by the integration of the mass density along the line of sight (Dhar and Williams, 2010; Lapi et al., 2012; Mo et al., 2010; Retana-Montenegro et al., 2012; Wright and Brainerd, 2000)

$$\Sigma(s)=\int_{-\infty}^{\infty}\rho(\vec{r})\,dz, \tag{3.7}$$

where $s = \sqrt{r^2 + z^2}$ is the projected radius (orthogonal to the line of sight) relative to the center. For a spherically symmetric density profile , we find that Eq. (3.7) can be also written in the following form (e.g., Lapi et al., 2012)

$$\Sigma(s) = 2\int_s^\infty \frac{r\rho(r)}{\sqrt{r^2 - s^2}} dr, \tag{3.8}$$

where one may recognize its special form as it is the Abel's integral equation.

Having defined the projected surface density we can infer the gravitational lens mass M_l, by carrying out an integration of the $\Sigma(s)$ over the disk which has radius s (see for example Eq. 41 in Retana-Montenegro et al., 2012)

$$M_l(s) = 2\pi \int_0^s x\Sigma(x)\, dx. \tag{3.9}$$

This quantity is the mass contained within an infinite cylinder of radius s in which the mass distribution is characterized by the mass density profile $\rho(\vec{r})$. Equation (2.10) cannot be solved independently, but must simultaneously satisfy Eq. (3.9), owing to the fact that one of the input parameters in Eq. (2.10) is the lens mass. Therefore, the relation between lens mass and halo mass that is needed in the computation of the lensing optical depth is derived only after solving this coupled nonlinear system.

3.2 Mass function

The computation of the lensing optical depth depends on the number density of lensing objects, which in our case are DM haloes. So, we need to obtain a formula that determines the distribution of virialized DM haloes (in the field) per volume element and per halo mass at a given redshift z, in order to estimate the lensing optical depth. This problem has been addressed by several authors in the past, either analytically (Bond et al., 1991; Pavlidou and Fields, 2005; Press and Schechter, 1974) or numerically (Jenkins et al., 2001; Tinker et al., 2008). All these works are based on the spherical collapse scenario (e.g., Gunn and Gott, 1972; Naderi et al., 2015). Improvements using ellipsoidal collapse do exist (e.g., Sheth et al., 2001), but we do not use them in this paper.

3.2.1 CDM mass function

The differential halo mass function of CDM haloes (the number of haloes with mass between the range M and $M + dM$ per proper volume at a given redshift) reads (Press and Schechter,

1974, see also Appendix A)

$$n(M,z) \equiv \frac{dN}{dM} = \sqrt{\frac{2}{\pi}} \frac{\rho_m(z)}{M} \frac{\delta_c(z)}{\sigma_M^2} \left| \frac{d\sigma_M}{dM} \right| \exp\left[-\frac{\delta_c^2(z)}{2\sigma_M^2} \right], \tag{3.10}$$

where M refers to the halo mass, z is the redshift, $\rho_m(z)$ is the mean matter density of the Universe at redshift z, and $\delta_c(z)$ denotes the overdensity of a structure collapsing at redshift z linearly extrapolated to the present. Moreover, σ_M is the rms of the density field smoothed on scale M. For an extensive description of all these quantities, as well as for exact formulae that determine these variables, we refer the reader to our Appendix A.

3.2.2 WDM mass function

Although the halo mass function for WDM haloes shows a similar behavior to the CDM one on galaxy clusters scales, it exhibits a cutoff below the dwarf galaxy scale, owing to the free streaming of WDM particles in the early Universe. The most commonly applied method to derive the WDM halo mass function is the development of N-body simulations that evolve the primordial density field perturbations in time, leading to collapsed DM haloes (e.g., Bose et al., 2016; Lovell, 2020a,b; Schneider et al., 2012). In this study, we choose to use the numerical fit offered by Lovell (2020b) to take into account the cutoff in the mass function of WDM haloes with respect to the CDM one. The halo mass function in the case of WDM is given by

$$n_{WDM}(M,z) = n_{CDM}(M,z) \left[1 + \left(\frac{\alpha M_{hm}}{M} \right)^{\beta} \right]^{\gamma}, \tag{3.11}$$

where M_{hm} is a characteristic mass scale (the half-mode mass), while α, β, γ are parameters of the fit that have been found to be $2.3, 0.8, -1$, respectively. The half-mode mass is associated with the free-streaming length which in turn is related to the rest mass of the WDM particle. In Fig. 3.1, we display the half-mode mass against the WDM particle mass, using the formula provided in Bose et al. (2016). For lighter WDM particles the half-mode mass increases remarkably due to the fact that the free-streaming length is higher. Current observations have ruled out the case where $m_{WDM} \lesssim 2.5$ keV.

Here, we are interested in exploring the case where the WDM is made of collision-less particles (thermal relics) of mass $m_{WDM} = 3.3$ keV. In this scenario, the theoretical value for the half-mode mass is $M_{hm} \simeq 2 \times 10^8\,\mathrm{M}_\odot$ (e.g., Bose et al., 2016). This value for the half-mode mass coincides with the one for the well-motivated sterile-neutrino model in which particles are assumed to have a rest mass equal to 7 keV and lepton asymmetry number

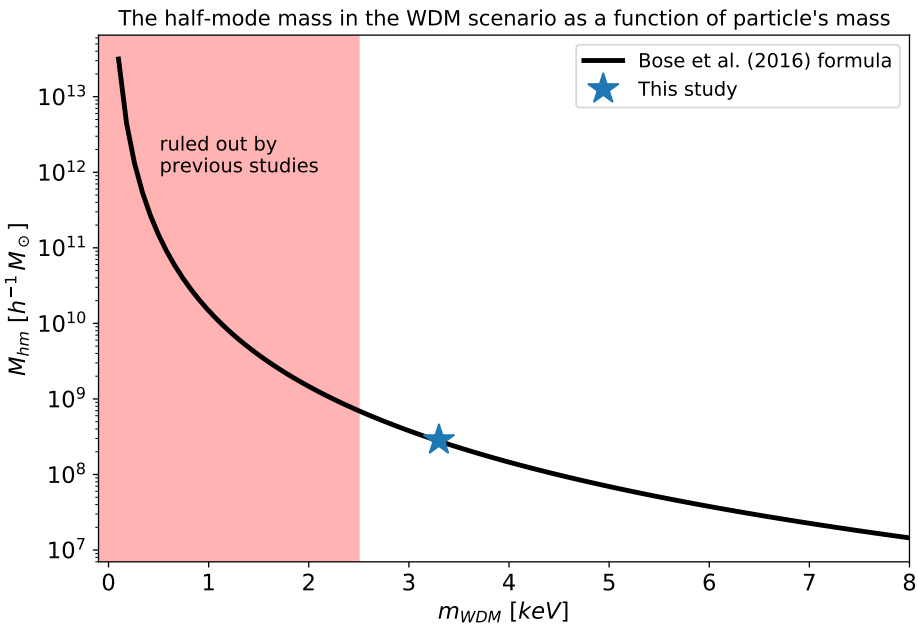

Fig. 3.1 Half-mode mass as a function of the WDM particle rest mass. Red zone shows the current constrained region of the parameter space. Blue star indicates the rest mass considered in this study. The formula that relates the half-mode mass to the rest mass is offered by Bose et al. (2016).

$L_6 = 8.66$ (see Bose et al., 2016). Sterile neutrinos are part of the neutrino Minimal Standard Model (νMSM; Boyarsky et al., 2009), which is a simple extension to the Standard Model of particle physics. It has been introduced to explain the unidentified 3.53 keV X-ray line observed recently in galaxies (see for example, Boyarsky et al., 2014) by considering this line to be the decay signal of those 7 keV sterile neutrinos.

Given that the cutoff in the halo mass function of these two WDM models is determined by the same half-mode mass and that the internal structure of haloes is identical, the inferences of this work concerning the 3.3 keV thermal relic WDM particle will also be valid for the 7 keV sterile neutrinos model. In Fig. 3.2, we display the differential halo mass function for the CDM model and for the WDM one investigated here as a function of the halo mass for various redshifts. Solid lines correspond to the proper density of haloes of mass M at different epochs (redshifts) divided by the present critical density of the Universe, whereas dashed lines represent the same quantities, but for WDM. A major difference between the CDM mass function and the mass function of WDM is that the latter one exhibits a cutoff at the dwarf-galaxy scales ($\sim 10^9$ $M_\odot$). This distinctive feature of the halo mass function in the WDM scenario has a considerable implication to the ability of DM haloes to act efficiently

as gravitational milli-lenses on background sources, because the mass function is directly involved in the calculation of the milli-lensing optical depth (Eq. 2.6).

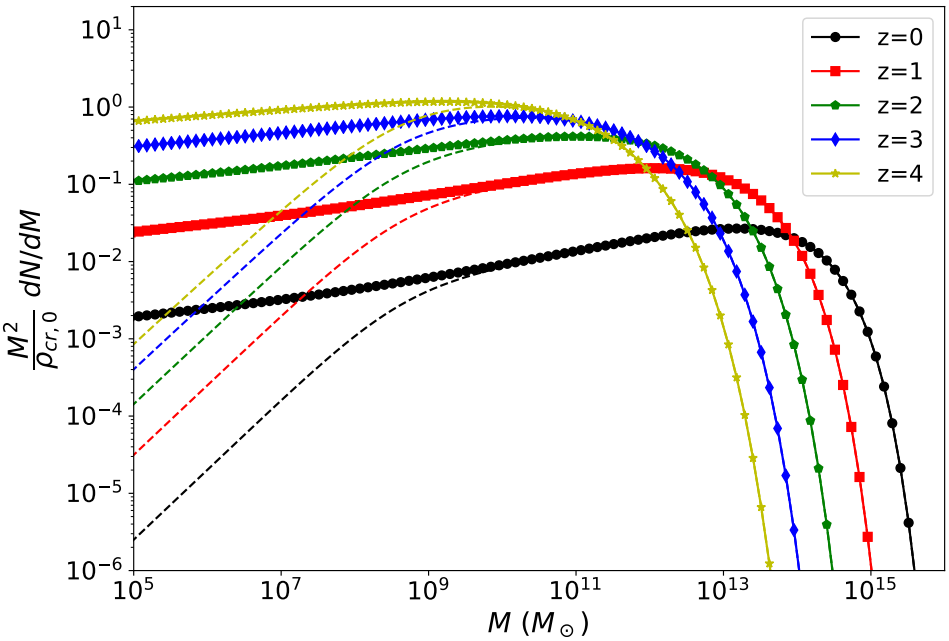

Fig. 3.2 Comparison of the CDM differential halo mass function with the one of the WDM model for various redshifts. Solid lines refer to CDM, while dashed lines correspond to WDM. The vertical axis corresponds to the halo mass while the y-axis shows the proper density of haloes of mass M normalized to the present value of the critical density of the Universe. Different colors correspond to different epochs (redshifts).

3.3 CDM halo density profile

To our knowledge, there are a couple of established spherically averaged mass density profiles that can successfully describe the distribution of CDM within a halo (see also Lazar et al. 2023). The first one is the so called Einasto profile, while the second one is the well-known Navarro-Frenk-White (NFW) profile. The major difference of the NFW profile from the Einasto one is that it predicts a cuspy halo's center, since the mass density declines to infinity as we approach the center of the halo, while in the Einasto profile the mass density is almost constant and finite near center. In this study, we employ the NFW profile for the description of the mass distribution within CDM haloes, as it is feasible to obtain analytical formulae for

the surface mass density and lens mass, as well. Though, for completeness we present both of them.

3.3.1 Einasto profile

The Einasto profile was firstly proposed by Einasto (1965) (see also, Cardone et al., 2005; Dhar and Williams, 2010; Merritt et al., 2006; Navarro et al., 2004; Retana-Montenegro et al., 2012) and has the following exponential form

$$\rho_E(r,c,r_{-2},a) = \rho_{-2}\exp\left[-2a^{-1}\left((r/r_{-2})^a - 1\right)\right], \tag{3.12}$$

where c is the concentration parameter, r_{-2} denotes the characteristic radius at which the logarithmic slope is equal to -2, and ρ_{-2} is the corresponding density. Such profile is characterized by a core in the innermost regions of the halo. Another form of this profile follows (see for example, Eq. 9 in Retana-Montenegro et al., 2012)

$$\rho_E(r,\rho_o,r_{-2},a) = \frac{200}{3}\rho_{cr}c^3\left(\frac{2}{a}\right)^{3/a}\frac{a}{\gamma(3/a,(2/a)c^a)}\cdot\exp\left[-(r/\ell)^a\right], \tag{3.13}$$

where the variable ℓ is equal to $r_{-2}(a/2)^a$, In addition, $\gamma(s,x)$ is an integral function known as the lower incomplete Gamma function, and is defined as

$$\gamma(s,x) = \int_0^x dt\, t^{s-1}e^{-t}. \tag{3.14}$$

Using Eq. (3.6) along with Eqs. (3.13), (3.14), we derive an expression for the enclosed mass $M_{enc}(r)$ within a sphere of radius r which turns out to be

$$M_{enc}(r) = M\frac{\gamma[3/a,(2/a)(r/r_{-2})^a]}{\gamma[3/a,(2/a)c^a]}, \tag{3.15}$$

while neither the lens' mass nor the surface mass density can be obtained analytically or even be written down in terms of elementary functions as Cardone et al. (2005) pointed out. Nevertheless, Dhar and Williams (2010) provide an impressively accurate numerical formula that fits the surface density pretty well, and hence can be implemented in studies with purposes similar to the ones in this work. The numerical fit for the surface mass density that is offered by Dhar & Williams (2010) is given below

$$\Sigma_E(s) = \frac{\Sigma_E(0)}{\Gamma(n+1)}\left\{n\Gamma\left[n,b(\zeta_2 X)^{1/n}\right] + \frac{b^n}{2}X^{1-1/2n}\gamma(1/2,X^{1/n})e^{-bX^{1/n}} - \delta b^n X e^{-b(\sqrt{1+\varepsilon^2}X)^{1/n}}\right\} \tag{3.16}$$

where

$$\Sigma_E(0) = 2r_{-2}\rho_o \frac{\Gamma(n+1)}{b^n} \tag{3.17}$$

$$\rho_o = \rho_{-2} e^{2/a} \tag{3.18}$$

$$b/2n = 1 \tag{3.19}$$

$$X = s/r_{-2} \tag{3.20}$$

$$\delta = (\zeta_2 - \zeta_1)\left[1 - e^{-X^\mu}\right] \tag{3.21}$$

$$\varepsilon = (\zeta_1 + \zeta_2)/2 \tag{3.22}$$

$$\zeta_1 = 1 \tag{3.23}$$

$$\zeta_2 = 1.1513 + \frac{0.05657}{n} - \frac{0.00903}{n^2} + \mathscr{O}(n^{-3}) \tag{3.24}$$

$$\mu = \frac{1.5096}{n} + \frac{0.82505}{n^2} - \frac{0.66299}{n^3} + \mathscr{O}(n^{-4}) \tag{3.25}$$

It should be noted that, the Einasto model consists of 3 free-parameters, which are the scale radius, r_{-2}, the concentration, c, and the $a(\equiv 1/n)$ parameter which controls the steepness of the density profile. However, Wang et al. (2020) concluded that this free parameter, a, should be equal to 0.16 in order for the density profile to be consistent with the data. In fact, they demonstrated that by keeping this parameter fixed at this value, they were able to fit the data (from N-body simulations) with high accuracy. Hence, Einasto profile turns out to be a two parameter density profile.

3.3.2 NFW profile

In this study, we employ the Navarro-Frenk-White (NFW) profile for the description of the mass distribution within CDM haloes (Navarro et al., 1995, 1996, 1997)

$$\rho(r, r_s, c, z) = \rho_{cr}(z) \frac{\phi_c}{(r/r_s)(1 + r/r_s)^2}, \tag{3.26}$$

where r_s is the characteristic radius, while ϕ_c is calculated by

$$\phi_c = \frac{200}{3} \frac{c^3}{\ln(1+c) - c/(1+c)}, \tag{3.27}$$

with c being the concentration parameter, which is not mass independent, but correlates strongly with the halo mass, as well as with the redshift, following a simple scaling law (see for example, Bullock et al., 2001; Dutton and Macciò, 2014; Klypin et al., 2016; Neto et al.,

2007; Prada et al., 2012; Ragagnin et al., 2019, 2021; Shan et al., 2017). The NFW profile predicts a cuspy halo's center, since the mass density goes as $\sim r^{-1}$ near the center of the halo.

Using Eq. (3.26) along with Eq. (3.6), we obtain the enclosed mass

$$M_{enc}\left(M,z,r_{200}(M,z)\right) = \frac{M}{\ln(1+c)-c/(1+c)} F(r,c,r_{200}), \tag{3.28}$$

where

$$F(r,c,r_{200}) = \ln(1+cr/r_{200}) - \frac{cr/r_{200}}{1+cr/r_{200}}. \tag{3.29}$$

From Eqs. (3.7) and (3.26), we obtain the surface density

$$\Sigma\left(s,M,z,r_{200}(M,z)\right) = 2\frac{\phi_c \rho_{cr}(z) r_{200} c^{-1}}{c^2(s/r_{200})^2-1} \mathscr{S}(s,c,r_{200}(M,z)), \tag{3.30}$$

where we have defined for convenience

$$\mathscr{S}\left(s,c,r_{200}(M,z)\right) = \begin{cases} 1-\dfrac{\cos^{-1}(r_{200}/cs)}{\sqrt{c^2(s/r_{200})^2-1}} & \text{if } s > r_s \\ 1-\dfrac{\cosh^{-1}(r_{200}/cs)}{\sqrt{1-c^2(s/r_{200})^2}} & \text{if } s < r_s \end{cases}. \tag{3.31}$$

From Eq. (3.9), the lens mass then is

$$M_{lens}\left(s,M,z,r_{200}(M,z)\right) = \frac{M}{\ln(1+c)-c/(1+c)} \mathscr{H}(s,c,r_{200}), \tag{3.32}$$

where

$$\begin{aligned} \mathscr{H}(s,c,r_{200}) &= \ln(cs/2r_{200}) \\ &+ \begin{cases} \dfrac{2}{\sqrt{(cs/r_{200})^2-1}} \arctan\sqrt{\dfrac{cs/r_{200}-1}{cs/r_{200}+1}} & \text{if } cs > r_{200} \\ 1 & \text{if } cs = r_{200} \\ \dfrac{2}{\sqrt{1-(cs/r_{200})^2}} \operatorname{arctanh}\sqrt{\dfrac{1-cs/r_{200}}{cs/r_{200}+1}} & \text{if } cs < r_{200} \end{cases}. \end{aligned} \tag{3.33}$$

3.4 WDM halo density profile

Warm dark matter is made of particles that had non-negligible thermal velocities at early times. This major difference is expected to have an impact on the concentration of mass

near the center, but not in the shape of the distribution of mass within a halo. Indeed, the density profile in WDM models can be well described by a NFW profile (see e.g., Bose et al., 2016; Lovell et al., 2014). However, DM haloes consisting of WDM are typically formed at smaller redshifts with respect to the formation of CDM haloes. This difference affects the concentration of the halo, which generally reflects the density of the Universe at the epoch of halo formation (for a detailed discussion see, Bose et al., 2016; Schneider et al., 2012; Zavala and Frenk, 2019). Therefore, we assume that the mass distribution in WDM haloes is consistent with the NFW profile, but more fuzzy, that is to say less concentrated around the center. In order to calculate the concentration parameter for WDM haloes as a function of the mass and the redshift we use the findings of Bose et al. (2016). They offer the following simple functional form for the concentration parameter

$$\frac{c_{WDM}}{c_{CDM}} = \left(1+\gamma_1 \frac{M_{hm}}{M}\right)^{-\gamma_2} (1+z)^{\beta(z)}, \tag{3.34}$$

where $\gamma_1 = 60$, $\gamma_2 = 0.17$, and $\beta(z) = 0.026z - 0.04$. M_{hm} is the half-mode mass and in this work is set to be $M_{hm} = 2 \times 10^8 M_\odot$ corresponding either to the model of thermal relics WDM particles of rest mass $m_{WDM} = 3.3$ keV or to the 7 keV sterile neutrinos model (an extension to the Standard model). Due to their smaller concentrations, WDM haloes will be less likely to exceed the lensing surface-density threshold, resulting in a lower milli-lensing optical depth.

3.5 SIDM halo density profile

3.5.1 SIDM core-like halo center

The SIDM model was originally introduced by Spergel and Steinhardt (2000) to explain observations of central densities in galaxies within the Local Group. Since then, numerous authors have argued that the self-interaction of particles leads to a core-like profile rather than a cusp-like profile. Such a feature could alleviate the "cusp-core" problem arising for CDM, and hence is considered a well motivated DM alternative.

There are two kinds of SIDM theories. In the first case the scattering rate per particle, $\Gamma(r)$, is velocity independent, which implies that the ratio of the effective cross section, σ, to the dark matter particle's mass, m, is constant (e.g., Elbert et al., 2015; Rocha et al., 2013). In the second scenario, the scattering rate is velocity dependent and falls rapidly as the velocity increases (e.g., Zavala et al., 2013). For a recent discussion on SIDM models, as well as on the observational constraints on the self-scattering cross section, see Tulin and Yu (2018).

In this work, we assume that the scattering rate per particle is velocity independent and has the following form

$$\Gamma(r) \propto \rho(r)(\sigma/m)v_{rms}(r), \tag{3.35}$$

where $\rho(r)$ is the DM mass density at radius r, while v_{rms} is the rms speed of dark matter particles. We consider a typical value for the ratio $\sigma/m \sim 1$ cm^2/g, since SIDM models with smaller values, on the order of 0.1 cm^2/g, are very similar to the CDM models even on scales smaller than dwarf galaxies and cannot produce detectable deviations from CDM predictions (Zavala et al., 2013). On the other hand, higher values of the cross section per mass, ~ 10 cm^2/g, have already been ruled out by cluster observations (see e.g., Dawson et al., 2012).

For the structure of SIDM haloes, we again assume spherical symmetry, but now we use a core-like profile. In fact, the mass density is well approximated by the Burkert profile (see Burkert, 1995), which also has two free parameters and is given by the following formula

$$\rho_B(r, r_b, \rho_b) = \frac{\rho_b}{(1 + r/r_b)\,(1 + (r/r_b)^2)}, \tag{3.36}$$

where r_b is the scale (core) radius, while ρ_b is the central density. As in the NFW profile, the free parameters of the Burkert profile scale with the halo mass. In the special case where $\sigma/m \sim 1$ cm^2/g, Rocha et al. (2013) have provided a couple of simple scaling laws that connect both the r_b and ρ_b with the halo mass, using data from N-body simulations. These relations (Eq. 17 and Eq. 20 in Rocha et al., 2013) are given below

$$\frac{r_b}{1\,\mathrm{kpc}} = 2.21 \left(\frac{M_{vir}}{10^{10}\,\mathrm{M}_\odot}\right)^{0.43}, \tag{3.37}$$

$$\frac{\rho_b}{\mathrm{M}_\odot/\mathrm{pc}^3} = 0.029 \left(\frac{M_{vir}}{10^{10}\,\mathrm{M}_\odot}\right)^{-0.19}. \tag{3.38}$$

Since these relations have been derived using the virial mass, M_{vir}, instead of M_{200} which we have employed throughout this work, we have to rescale the density profile to be consistent with Eq. (3.2). Equation (3.36) can be recast as

$$\rho_B(r, M) = \mathscr{A}(M)\frac{\rho_b}{(1 + r/r_b)\,(1 + (r/r_b)^2)}, \tag{3.39}$$

where

$$\mathscr{A}(M) = \frac{M r_b^{-3}}{2\pi\rho_b}\left[\ln\left(1 + \frac{r_{200}}{r_b}\right) + \frac{1}{2}\ln\left(1 + \frac{r_{200}^2}{r_b^2}\right) - \tan^{-1}\left(\frac{r_{200}}{r_b}\right)\right]^{-1}, \tag{3.40}$$

and now we can use the halo mass $M \equiv M_{200}$ instead of the virial mass in Eqs. (3.37), (3.38). The term $\mathscr{A}(M)$ has been derived by requiring the mean density inside a sphere of radius r_{200} to be $200\rho_{cr}$ (see Eq. 3.2).

Using Eqs. (3.6) and (3.39), we obtain for the enclosed mass

$$M_{enc}(r) = \mathscr{A}(M)\pi\rho_b r_b^3 \left[\ln\left(1+\frac{r^2}{r_b^2}\right) + 2\ln\left(1+\frac{r}{r_b}\right) - 2\tan^{-1}\left(\frac{r}{r_b}\right)\right]. \tag{3.41}$$

The surface density cannot in general be derived analytically and therefore we have to perform the integration numerically. In the special case where $s = 0$, that is for the column density through the line of sight, the integration that returns the surface density $\Sigma_B(0)$ yields the closed-form expression

$$\Sigma_B(s=0,M) = \mathscr{A}(M)\frac{\pi}{2}\rho_b r_b, \tag{3.42}$$

where the index B indicates that this surface density arises from the Burkert profile. The surface mass density is maximized when $s = 0$, since $\rho(r)$ is a monotonically decreasing function of r, and as a result for a SIDM halo of given mass, the maximum value of the surface density is determined by Eq. (3.42). This feature is of great importance in strong gravitational lensing where the surface density must exceed a critical threshold in order to significantly bend a light ray.

In order to have a qualitative picture of the differences between the three mass density profiles mentioned above, in Fig. 3.3, we apply them to a DM halo of mass $M = 10^8\ \mathrm{M}_\odot$ at redshift $z = 0$. For SIDM particles the density profile near the center is flat, while for CDM particles the profile near the center goes as r^{-1}, since we have used the NFW profile. For WDM particles the profile is NFW-like but with larger characteristic radius than in the CDM reflecting the fact that the concentration in the WDM scenario is smaller than the one in CDM.

3.5.2 SIDM core collapse

Even though most of SIDM models are in favor of a less dense core-like halo center, the strong self-interaction developed between particles in the innermost region of the halo might have important implications in the dynamical evolution of the halo. In one scenario, strong self-interactions between particles induce a negative heat capacity, eventually leading to the formation of a dense central core in the inner part of the halo (see e.g., Yang and Yu, 2021, 2022). Yang and Yu (2021) demonstrated that such a scenario can be successful in explaining the observational excess of small-scale gravitational lenses in galaxy clusters reported in

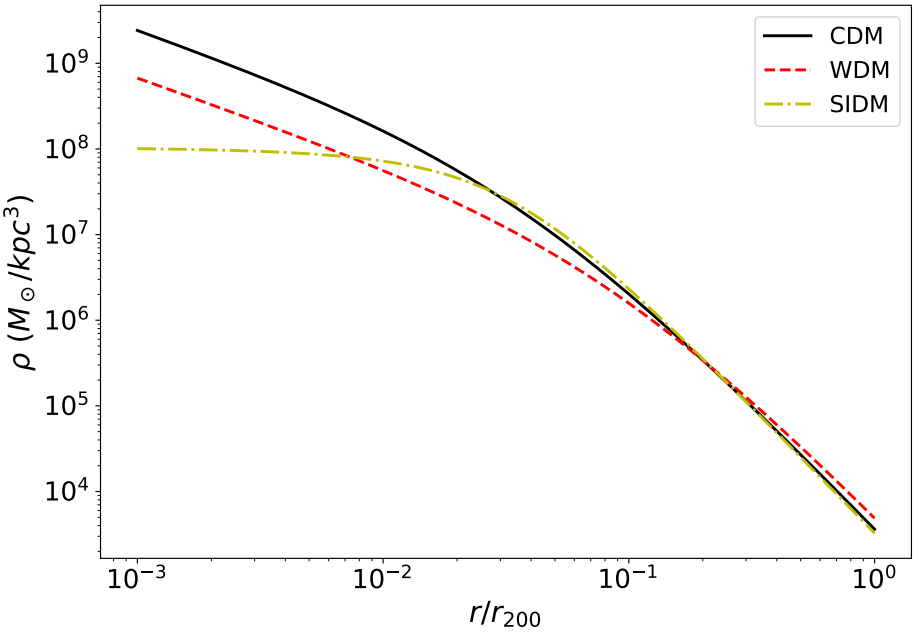

Fig. 3.3 Comparison of mass density profiles for a given halo of mass $M = 10^8\,\mathrm{M}_\odot$ at redshift $z = 0$ for various dark matter scenarios. The concentration for the CDM case is given by Eq. (4.1). Black solid line represents the CDM density profile, while the red-dashed line corresponds to the WDM one (with $M_{hm} = 2 \times 10^8\ \mathrm{M}_\odot$). The yellow dot-dashed line stands for the SIDM model.

Meneghetti et al. (2020). They exploited the fact that at late stages of the gravothermal evolution of a halo composed of SIDM, the core might undergo gravothermal collapse, resulting in a highly dense halo center, thereby increasing its lensing effect on background sources compared to CDM haloes.

In the most extreme case, the collapsed core can further contract, eventually leading to the formation of a supermassive black hole (SMBH) at the halo center. This scenario was firstly proposed and studied extensively by Feng et al. (2021) (see also Feng et al., 2022) as a possible mechanism to explain the existence and origin of SMBHs at high redshifts ($z \sim 6-7$). Essentially, SIDM offers a natural mechanism for triggering dynamical instability, a necessary condition to form a black hole. This scenario can be tested and well-constrained through milli-lensing, since the central SMBH can effectively act as a strong gravitational lens and produce multiple images of a compact background source.

Given that studies dealing with the core collapse scenario do not provide an exact formula for the final mass distribution of DM inside the collapsed halo, we shall restrict ourselves in

investigating here only the latter, most extreme, scenario of core collapse where the formation of a SMBH takes place from the gravothermal collapse of the core. The exploration of this model yields an upper limit on the expectation value of lensing events in the SMILE source sample in the case of the SIDM scenario.

Chapter 4

Results

4.1 CDM

4.1.1 CDM: model A

We start by investigating the CDM scenario using a concentration-mass relation derived from N-body simulations. We employ the relation given in Ragagnin et al. (2019) to determine the dependence of the concentration parameter c on the redshift z, as well as on the halo mass M:

$$c(M,z) = 6.02 \left(\frac{M}{10^{13}\,\mathrm{M}_\odot} \right)^{-0.12} \left(\frac{1.47}{1+z} \right)^{0.16} . \tag{4.1}$$

In Fig. 4.2 we plot with a blue solid line the milli-lensing optical depth obtained for this c(M,z). The value of the milli-lensing optical depth is well below $\sim 10^{-4}$ implying that even a sample of ten thousands distant ($z \sim 5$) compact sources is highly unlikely to produce at least one lensing event. Indeed, performing the summation in Eq. (2.12) over all sources involved in the SMILE sample, we end up with the value $\langle N_{exp} \rangle \simeq 1.5 \times 10^{-3}$, which makes detection of a milli-lens improbable.

4.1.2 CDM: model B

As a limiting case of the possible effect of the concentration-mass relation on our results, we also test a power-law extrapolation to lower masses of the empirical (fitted from observations rather than simulations) c-M relation shown in Fig. 13 of Prada et al. (2012)

$$\log c(M,z) = 4.23 - 0.25 \log(M/M_\odot) - 0.16 \log \left(\frac{1+z}{1.47} \right) . \tag{4.2}$$

Regarding the dependence on redshift, we consider that it is identical to Eq. (4.1), but we stress that most studies suggest a weak dependence of the concentration on redshift, so even if we slightly modify the last term in Eq. (4.2) associated with the redshift dependence, the overall results do not change noticeably. In practice, the concentration parameter is set by the halo mass. We note that Eq. (4.2) predicts higher values of the concentration parameter with respect to the ones inferred from N-body simulations. Although this $c-M$ relation has been derived from galaxy cluster observations and might overestimate the c parameter of haloes on subgalactic scales, recently Şengül and Dvorkin (2022) investigated the strong lens system JVAS B1938+666, concluding that subgalactic DM haloes can be highly concentrated ($c \approx 60$), in line with Eq. (4.2).

Using this relation in Eq. (2.6), we obtain the green dash-dotted line in Fig. 4.2, showing the milli-lensing optical depth as a function of the source redshift. Subsequently, using Eq. (2.12) to compute the expectation value of lensing events in the source sample of SMILE, we obtain $\langle N_{exp} \rangle \simeq 1.2$. This value deviates remarkably from the one corresponding to model A (see Sect. 4.1.1), demonstrating that the concentration-mass relation plays a crucial role in the process of strong gravitational milli-lensing and can thus be strongly constrained with milli-lensing observations. This value also places an upper limit on the expectation number of detected milli-lenses in the SMILE's source sample, in the case where the properties of DM particles are in line with the framework of the CDM model.

A comparison between the two concentration-mass relations related to the CDM scenario for redshift $z = 0$ can be found in Fig. 4.1. The concentration-mass relation given by Eq. (4.1) (Model A) is displayed with a blue solid line, while the green dash-dotted line stands for the $c(M)$ considered in model B (i.e., Eq. 4.2).

4.2 SIDM

In the SIDM model, there are two possibilities, which lead to quite different internal structure of haloes. The first corresponds to haloes described by a core-like density profile, while the latter refers to haloes of collapsed cores.

4.2.1 SIDM core-like halo center

The standard scenario is the one where the inner part of haloes is characterized by a core-like profile yielding the projected surface mass density of Eq. (3.42). Since the surface mass density is maximized at the center of the halo (as long as the density profile is a decreasing function of r), if the central region does not exceed the critical threshold for strong lensing,

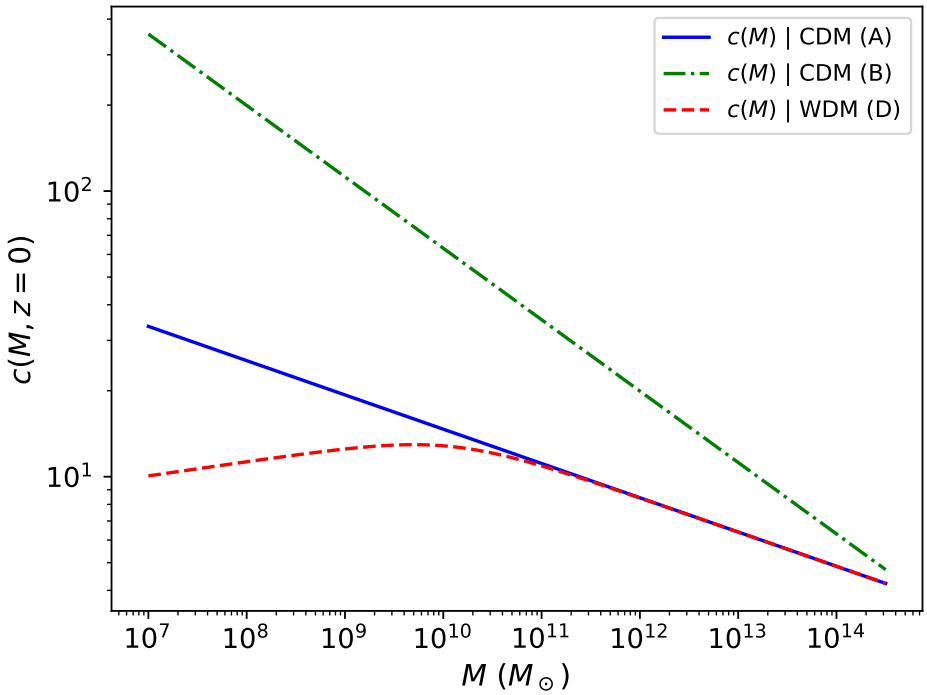

Fig. 4.1 Concentration-mass relation at $z = 0$ for different dark matter scenarios. Blue solid line represents the CDM (A) scenario in which the concentration-mass relation is given by Eq. (4.1). Green dash-dotted line stands for the (B) CDM model in which the concentration-mass relation is Eq. (4.2). Red dashed line refers to WDM model (D) where $c(M,z)$ is calculated by Eq. (3.34).

then the halo will not act as a strong lens. Using Eq. (3.42) and Eq. (2.9), we conclude that the halo mass of a SIDM halo must be $\gtrsim 10^{14}\,\mathrm{M}_\odot$, for the surface mass density at the center to exceed the strong lensing threshold. However, this mass scale corresponds to galaxy clusters and therefore no trustful inferences can be done without including the effect of strong lensing due to the presence of baryons. The main finding is that SIDM-only subgalactic haloes cannot produce milli-lensing images since they are not dense enough to satisfy the strong lensing criterion.

4.2.2 SIDM core collapse: model C

The second scenario related to SIDM haloes is based on the gravothermal core collapse process that might take place in the inner parts of SIDM haloes (see Sect. 3.5.2). Assuming that the halo in the beginning was described by a NFW profile with the concentration-mass relation to given by Eq. (4.1), we can calculate the mass enclosed inside a projected disk

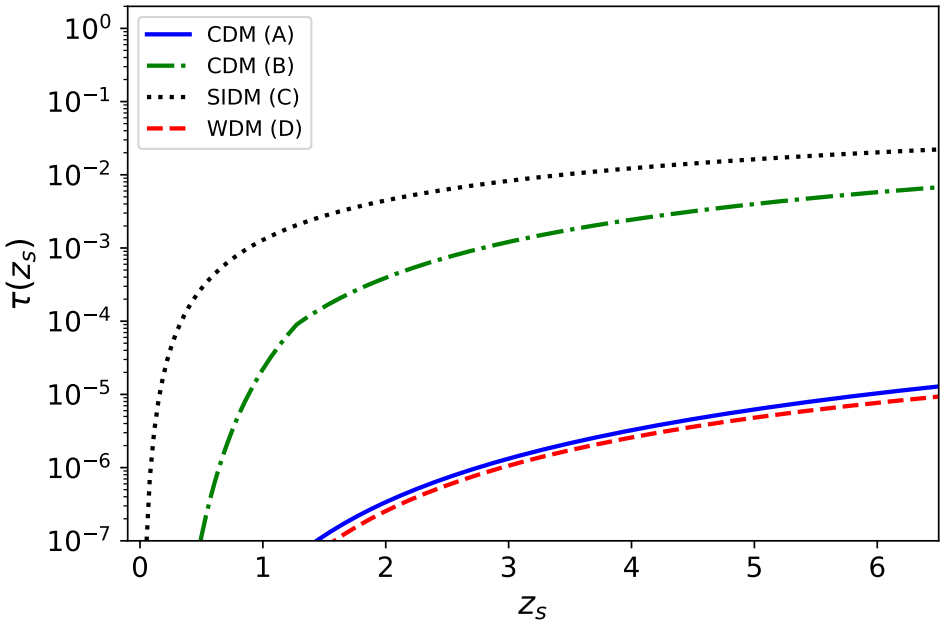

Fig. 4.2 Lensing optical depth as a function of the source redshift for different dark matter scenarios: CDM (A) model (blue solid line); CDM (B) model (green dot-dashed line); SIDM core-collapse (C) model (black dotted line); and WDM (D) model (red dashed line).

with radius equal to the scale radius r_s. Then, we consider the most extreme case where the entire core collapses into a very small but extremely dense core that eventually results in the formation of a compact object. This collapsed core is the part of the halo that can produce strong gravitational lensing of light emitted by background sources.

In Fig. 4.2, we show with the black dotted line the milli-lensing optical depth in the case of SIDM core collapse. Having obtained the optical depth, we carry out the sum shown in Eq. (2.12) over the redshifts of the SMILE project sources and find the value $\langle N_{exp} \rangle \simeq 13$.

4.3 WDM: model D

In order to derive the milli-lensing optical depth for the scenario of WDM, where particles are supposed to have a rest mass $m_{WDM} = 3.3\,\text{keV}$ (thermal relic) or be sterile neutrinos with a rest mass equal to $7\,\text{keV}$, we take into account that the halo mass function is different from that in CDM, and so we adopt the fit offered by Lovell (2020b) (Eq. 3.11) to model the cosmological abundance of WDM haloes in the field. Regarding the density profile we again employ the NFW one, but with the concentration parameter to be given by Eq.

(3.34). This concentration-mass relation is however a fit that relates the concentration of WDM haloes with the one corresponding to CDM haloes, so we simply consider that the concentration-mass relation of CDM haloes is the one shown in Eq. (4.1) and in such a way we obtain a formula for the concentration of WDM haloes as a function of the halo mass and redshift. In Fig. 4.1, we display the concentration-mass relation which corresponds to WDM haloes at $z = 0$ with a red dashed line.

Performing the integration of Eq. (2.6), we find the milli-lensing optical depth in the case of WDM, shown in Fig. 4.2 with the red dashed line. Combining this result with Eq. (2.12), we compute the expectation number of detected WDM milli-lenses, obtaining $\langle N_{exp} \rangle \simeq 1.1 \times 10^{-3}$. It is therefore extremely unlikely to detect any milli-lenses with SMILE if DM is in the form of WDM.

Chapter 5

Discussion & conclusions

In this work we have explored the ability of subgalactic DM haloes to act as milli-lenses on background sources resulting in multiple images of the same source with angular separation on the order of milli-arcseconds, considering different DM models. We have developed a semi-analytical method to estimate the expectation value of detected milli-lenses in several DM scenarios, computing the lensing optical depth. We have modeled the number density and internal structure of haloes using either (semi)analytical calculations or fits to N-body simulation results, depending on the DM model. We have restricted ourselves in applying the point-mass lens approximation to infer the lens mass, imposing the effective surface threshold criterion for strong lensing to connect the lens mass to the halo mass. Finally, we used the milli-lensing optical depth in each scenario to calculate the expectation number of detected milli-lenses in the source sample of the SMILE project.

We found that the probability of strong milli-lensing by DM haloes strongly depends on the model, being regulated by the properties of DM particles which dictate the inner structure of haloes, as well as their number density. We have shown that even within the CDM model, the lensing optical depth is quite sensitive to variations in the concentration-mass relation, in agreement with Amorisco et al. (2022), leading to very different expectation values of detected milli-lenses in the SMILE source sample. Milli-lensing observations might therefore enable us to constrain the concentration-mass relation down to subgalactic mass scales.

In addition, we have demonstrated that DM scenarios which are in favor of core-like density profiles, such as the SIDM one investigated here, are unlikely to produce milli-lenses because they predict haloes with low-density centers. However, our method allows to also probe scenarios like core collapse which enhance considerably the probability of milli-lensing.

Finally, we have shown that haloes consisting of WDM lead to an extremely small milli-lensing optical depth due to their combination of low concentration and mass-function

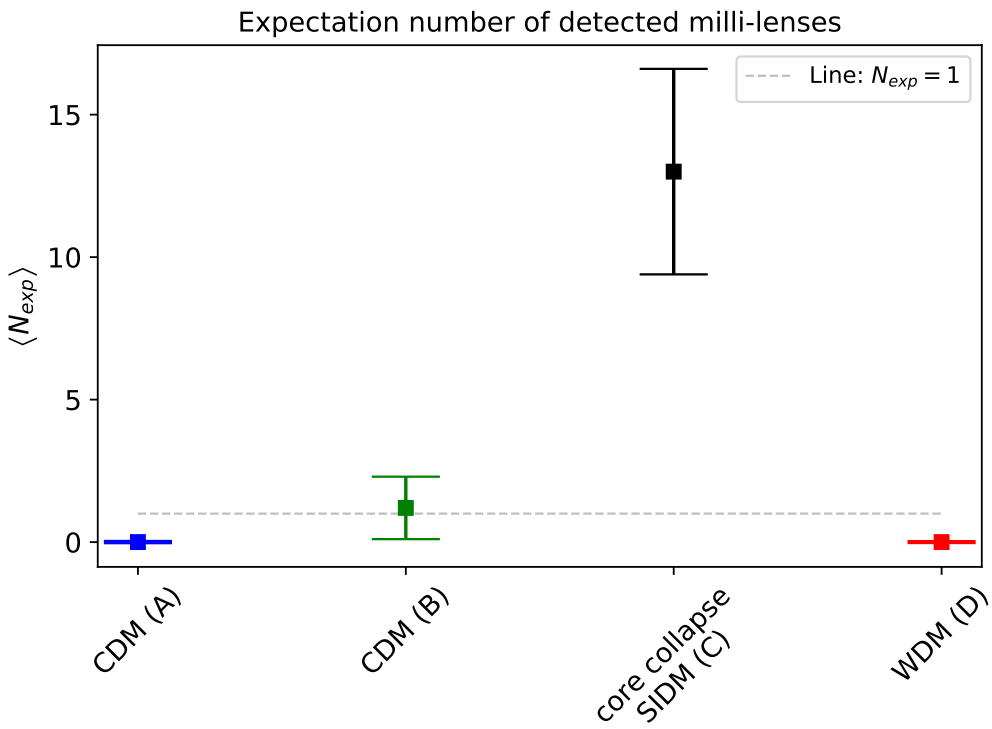

Fig. 5.1 Expectation number of detected milli-lenses in the SMILE project. Colored points refer to different DM models: (A) CDM (blue); (B) CDM (green); (C) SIDM core-collapse (black); and (D) WDM (red). The error-bars have been derived assuming Poisson-like error in the calculation of the expectation values.

cutoff. Even if a steeper concentration-mass relation (such as Eq. 4.2) is used, the cutoff in the number density below subgalactic scales still prevent the milli-lensing optical depth from increasing significantly. Therefore, the detection of milli-lenses would provide definitive evidence against the WDM model and more generally models that exhibit a cutoff in their halo mass function affecting the $10^6 - 10^9$ $M_\odot$ mass scales.

In Fig. 5.1, we summarize our results, plotting the expectation value of detected milli-lenses for all models investigated in this study. The blue point corresponds to the CDM model A (Sect. 4.1.1), while the green point refers to the CDM model B (Sect. 4.1.2). The black point corresponds to the core collapse SIDM scenario C (Sect. 4.2.2) and the red point to the WDM model D (Sect. 4.3). Even among the limited number of DM models studied here, milli-lensing observations of source samples comparable to that of SMILE hold significant discriminating power.

5.1 Potential sources of uncertainty

5.1.1 Contribution of baryons

Even though subgalactic haloes are expected to be almost empty of baryons, one source of uncertainty in our work might be the fact that we ignore the overall effect of baryons in the internal structure of haloes, which in principle can alter the ability of those haloes to act as milli-lenses. Although such systems are DM dominated, the baryons might play a crucial role in the strong lensing and therefore it is left for a future investigation, since the purpose of this paper is mostly to highlight the point that milli-lensing observations can be used to constrain the nature of dark matter and further discriminate between currently viable models.

5.1.2 Contribution of super-massive black holes

Another possible source of uncertainty arises from the fact that some DM haloes might host a SMBH at their center, which would contribute significantly in the strong lensing signal from those haloes, thereby modifying our results. However, neither the fraction of haloes that host such objects at their centers nor the accurate relation between SMBH and halo mass are known. In addition, there is still much discussion on explaining the existence of unexpectedly large SMBHs in luminous quasars observed at high redshifts, which might challenge current theoretical models.

In general milli-lensing experiments, and in particular the upcoming results of the SMILE project (see Sect. 2.3), could be exploited to test theoretical models of SMBH formation in the early Universe through their imprints on milli-lensing signals, and thus milli-lensing surveys might have strong discriminatory power in this context. Nevertheless, this issue requires very careful and detailed treatment in modeling the connection of DM haloes to SMBHs that are embedded inside them, and therefore will be addressed in a future paper. Hence we do not take this possibility into account and ignore the effect of SMBHs in this study.

5.1.3 Sensitivity to the redshift distribution

Here, we made a rather conservative choice and assumed a certain redshift distribution for the $\sim 1/3$ of sources for which no redshift measurements were currently available. Given the lack of knowledge about the distances of these sources, we adapted a rather plausible redshift distribution, which was chosen to be similar to the one of the sources with known redshift. This conservative choice partially affects the results, although not our qualitative conclusions.

For instance, if we considered that a considerable fraction of sources with missing redshift measurements are among the weakest and most distant sources, then the expectation number of detected milli-lenses would increase. In this case, the constraints computed in this study would be lower limits.

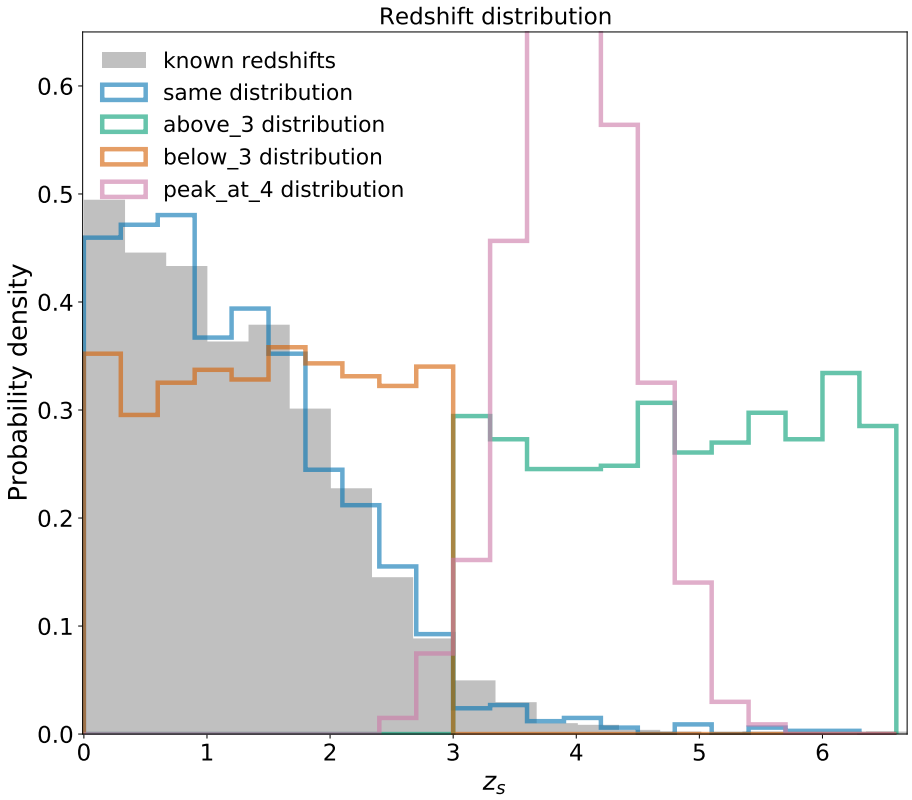

Fig. 5.2 Redshift distribution of the total number of sources in the SMILE sample. In light grey the redshift distribution of sources with known redshift (Euclid future measurements are not considered). In colors, four different hypothetic redshift distributions for sources with unknown redshift: a redshift distribution similar to that of sources with known redshift (blue), a uniform distribution between $z = 0$ and $z = 3$ (orange), a uniform distribution between $z = 3$ and z_{max} in our sample (green), and a Gaussian distribution around $z = 4$ (pink), justified by recent finding on radio-loud sources (Sbarrato et al., 2022).

To quantify the effect of the redshift distribution in our findings, we re-computed the expectation value of detected milli-lenses in SMILE, for the four representative DM models discussed in Ch. 4, considering four different redshift distributions for sources with currently unknown redshift. In Fig. 5.2, we display the redshift distribution of the sources with known redshift (light grey color) along with four hypothetical redshift distributions for the SMILE sources of currently missing redshift. Blue line corresponds to a redshift distribution similar to the one of sources with known redshift, orange line refers to a uniform distribution between

$z_s = 0$ and $z_s = 3$, green line stands for a uniform distribution between $z_s = 3$ and z_{max} (in the SMILE sample), and pink line is a Gaussian distribution around $z_s = 4$, motivated by the recent findings on radio-loud sources (Sbarrato et al., 2022).

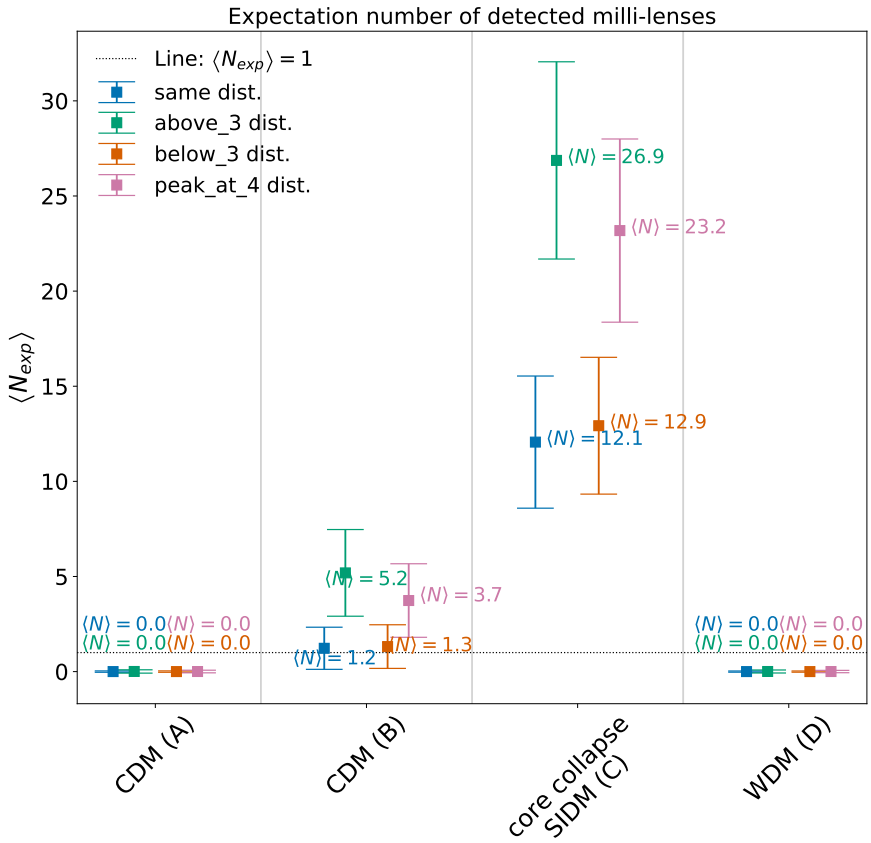

Fig. 5.3 Expectation values of detected milli-lenses within SMILE for all different redshift distributions shown in Fig. 5.2 and for four different DM scenarios considered in this study (see Ch. 4).

In Fig. 5.3, we plot the computed expectation value of detected milli-lenses for the aforementioned different redshift distributions of the sources of missing redshift (see Fig. 5.2). Two DM models (B and C) predict the detection of milli-lens systems within the SMILE project, while the other two scenarios (A and D) predict numbers that are below the detection threshold. This means that, irrespective of the redshift distribution, both in the case in which no milli-lens system is found and in the case in which we find some, we will be able to discard some of the current DM models. Nevertheless, the redshift distribution yields a measurable variation in the expectation values, as clearly shown in Fig. 5.3. In model (B) the expectation number spans from ~ 1 to ~ 5, for different redshift distributions, and for model (C) from ~ 11 to ~ 27. Hence, better estimates of the expectation values of detected milli-lenses can

be only obtained by increasing the number of sources with measured redshifts in the future. *Obtaining redshift measurements for the SMILE sources of currently missing redshift would therefore be a critical step for the SMILE project*.

It should be noted, however, that the qualitative findings in this work are insensitive in variations of the redshift distribution corresponding to the fraction of sources with unknown distances. As a matter of fact, even if we considered that all sources of unknown redshift (~ 1600) had a redshift at about 5, then as can be inferred from Fig. 4.2, the lensing optical depth for the models (A) & (D), which predict zero milli-lenses, would still be well-below $\sim 10^{-4}$, therefore could not yield measurable deviations in the expectation values, which would again vanish for these two models.

5.2 Summary

In this study, we have concluded that: 1) the source sample included in the SMILE project is sufficiently large to enable inferences about the nature of DM; 2) WDM haloes are highly unlikely to produce even a single strong milli-lensing event in the source sample of SMILE; 3) SIDM haloes can only act as strong milli-lenses in the case where self-interactions trigger the core collapse mechanism, leading to highly dense cores; 4) the ability of CDM subgalactic haloes to act as milli-lenses strongly depends on the mass-concentration relation; and 5) gaining information towards the cosmological distances of the SMILE sources of currently missing redshift is a critical step towards obtaining more robust estimates of the expectation value of detected milli-lenses. Finally, we have shown that if CDM is indeed the relevant model for describing the properties of DM particles, then milli-lensing observations will enable us to further constrain the relationship between concentration and halo mass down to subgalactic mass scales.

In short, we have demonstrated that milli-lensing surveys allow us to probe the properties of DM particles and infer constrains on their nature. Hopefully, the completion of the SMILE project (see Sect. 2.3) in combination with this thesis, as well as follow up theoretical works on the calculation of the milli-lensing optical depth, including the effects of baryons, will give us the unique opportunity to explore the nature of dark matter and do considerable progress towards its identification.

References

Amorisco, N. C., Nightingale, J., He, Q., Amvrosiadis, A., Cao, X., Cole, S., Etherington, A., Frenk, C. S., Li, R., Massey, R., and Robertson, A. (2022). Halo concentration strengthens dark matter constraints in galaxy-galaxy strong lensing analyses. *MNRAS*, 510(2):2464–2479.

Benitez-Llambay, A. and Frenk, C. (2020). The detailed structure and the onset of galaxy formation in low-mass gaseous dark matter haloes. *MNRAS*, 498(4):4887–4900.

Bond, J. R., Cole, S., Efstathiou, G., and Kaiser, N. (1991). Excursion Set Mass Functions for Hierarchical Gaussian Fluctuations. *ApJ*, 379:440.

Bond, J. R. and Efstathiou, G. (1984). Cosmic background radiation anisotropies in universes dominated by nonbaryonic dark matter. *ApJ*, 285:L45–L48.

Bose, S., Hellwing, W. A., Frenk, C. S., Jenkins, A., Lovell, M. R., Helly, J. C., and Li, B. (2016). The Copernicus Complexio: statistical properties of warm dark matter haloes. *MNRAS*, 455(1):318–333.

Bosma, A. (1981). 21-cm line studies of spiral galaxies. I. Observations of the galaxies NGC 5033, 3198, 5055, 2841, and 7331. *AJ*, 86:1791–1824.

Boyarsky, A., Ruchayskiy, O., Iakubovskyi, D., and Franse, J. (2014). Unidentified Line in X-Ray Spectra of the Andromeda Galaxy and Perseus Galaxy Cluster. *Phys. Rev. Lett.*, 113(25):251301.

Boyarsky, A., Ruchayskiy, O., and Shaposhnikov, M. (2009). The Role of Sterile Neutrinos in Cosmology and Astrophysics. *Annual Review of Nuclear and Particle Science*, 59(1):191–214.

Browne, I. W. A., Wilkinson, P. N., Jackson, N. J. F., Myers, S. T., Fassnacht, C. D., Koopmans, L. V. E., Marlow, D. R., Norbury, M., Rusin, D., Sykes, C. M., Biggs, A. D., Blandford, R. D., de Bruyn, A. G., Chae, K. H., Helbig, P., King, L. J., McKean, J. P., Pearson, T. J., Phillips, P. M., Readhead, A. C. S., Xanthopoulos, E., and York, T. (2003). The Cosmic Lens All-Sky Survey - II. Gravitational lens candidate selection and follow-up. *MNRAS*, 341(1):13–32.

Bryan, G. L. and Norman, M. L. (1998). Statistical Properties of X-Ray Clusters: Analytic and Numerical Comparisons. *ApJ*, 495(1):80–99.

Bullock, J. S. and Boylan-Kolchin, M. (2017). Small-Scale Challenges to the ΛCDM Paradigm. *ARA&A*, 55(1):343–387.

Bullock, J. S., Kolatt, T. S., Sigad, Y., Somerville, R. S., Kravtsov, A. V., Klypin, A. A., Primack, J. R., and Dekel, A. (2001). Profiles of dark haloes: evolution, scatter and environment. *MNRAS*, 321(3):559–575.

Burkert, A. (1995). The Structure of Dark Matter Halos in Dwarf Galaxies. *ApJ*, 447:L25–L28.

Cardone, V. F., Piedipalumbo, E., and Tortora, C. (2005). Spherical galaxy models with power-law logarithmic slope. *MNRAS*, 358(4):1325–1336.

Casadio, C., Blinov, D., Readhead, A. C. S., Browne, I. W. A., Wilkinson, P. N., Hovatta, T., Mandarakas, N., Pavlidou, V., Tassis, K., Vedantham, H. K., Zensus, J. A., Diamantopoulos, V., Dolapsaki, K. E., Gkimisi, K., Kalaitzidakis, G., Mastorakis, M., Nikolaou, K., Ntormousi, E., Pelgrims, V., and Psarras, K. (2021). SMILE: Search for MIlli-LEnses. *MNRAS*, 507(1):L6–L10.

Cline, J. M. (2021). Dark atoms and composite dark matter. *arXiv e-prints*, page arXiv:2108.10314.

Cole, S. and Lacey, C. (1996). The structure of dark matter haloes in hierarchical clustering models. *MNRAS*, 281:716.

Condon, J. J., Cotton, W. D., Greisen, E. W., Yin, Q. F., Perley, R. A., Taylor, G. B., and Broderick, J. J. (1998). The NRAO VLA Sky Survey. *AJ*, 115(5):1693–1716.

Corbelli, E. and Salucci, P. (2000). The extended rotation curve and the dark matter halo of M33. *MNRAS*, 311(2):441–447.

Şengül, A. Ç. and Dvorkin, C. (2022). Probing dark matter with strong gravitational lensing through an effective density slope. *MNRAS*, 516(1):336–357.

Cuesta, A. J., Prada, F., Klypin, A., and Moles, M. (2008). The virialized mass of dark matter haloes. *MNRAS*, 389(1):385–397.

Cyburt, R. H., Fields, B. D., Olive, K. A., and Yeh, T.-H. (2016). Big bang nucleosynthesis: Present status. *Reviews of Modern Physics*, 88(1):015004.

Dawson, W. A., Wittman, D., Jee, M. J., Gee, P., Hughes, J. P., Tyson, J. A., Schmidt, S., Thorman, P., Bradač, M., Miyazaki, S., Lemaux, B., Utsumi, Y., and Margoniner, V. E. (2012). Discovery of a Dissociative Galaxy Cluster Merger with Large Physical Separation. *ApJ*, 747(2):L42.

Dhar, B. K. and Williams, L. L. R. (2010). Surface mass density of the Einasto family of dark matter haloes: are they Sersic-like? *MNRAS*, 405(1):340–346.

Dutton, A. A. and Macciò, A. V. (2014). Cold dark matter haloes in the Planck era: evolution of structural parameters for Einasto and NFW profiles. *MNRAS*, 441(4):3359–3374.

Einasto, J. (1965). On the Construction of a Composite Model for the Galaxy and on the Determination of the System of Galactic Parameters. *Trudy Astrofizicheskogo Instituta Alma-Ata*, 5:87–100.

Elbert, O. D., Bullock, J. S., Garrison-Kimmel, S., Rocha, M., Oñorbe, J., and Peter, A. H. G. (2015). Core formation in dwarf haloes with self-interacting dark matter: no fine-tuning necessary. *MNRAS*, 453(1):29–37.

Faber, S. M. and Jackson, R. E. (1976). Velocity dispersions and mass-to-light ratios for elliptical galaxies. *ApJ*, 204:668–683.

Feng, W.-X., Yu, H.-B., and Zhong, Y.-M. (2021). Seeding Supermassive Black Holes with Self-interacting Dark Matter: A Unified Scenario with Baryons. *ApJ*, 914(2):L26.

Feng, W.-X., Yu, H.-B., and Zhong, Y.-M. (2022). Dynamical instability of collapsed dark matter halos. *J. Cosmology Astropart. Phys.*, 2022(5):036.

Gao, H.-X., Geng, J.-J., Hu, L., Hu, M.-K., Lan, G.-X., Chang, C.-M., Zhang, S.-B., Zhang, X.-L., Huang, Y.-F., and Wu, X.-F. (2022). Gravitationally lensed orphan afterglows of gamma-ray bursts. *MNRAS*, 516(1):453–464.

Gregory, P. C., Scott, W. K., Douglas, K., and Condon, J. J. (1996). The GB6 Catalog of Radio Sources. *ApJS*, 103:427.

Gunn, J. E. and Gott, J. R. (1972). On the Infall of Matter Into Clusters of Galaxies and Some Effects on Their Evolution. *ApJ*, 176:1.

Guo, X. and Lu, Y. (2022). Probing the nature of dark matter via gravitational waves lensed by small dark matter halos. *Phys. Rev. D*, 106(2):023018.

Jenkins, A., Frenk, C. S., White, S. D. M., Colberg, J. M., Cole, S., Evrard, A. E., Couchman, H. M. P., and Yoshida, N. (2001). The mass function of dark matter haloes. *MNRAS*, 321(2):372–384.

Kalantari, Z., Ibrahim, A., Reza Rahimi Tabar, M., and Rahvar, S. (2021). Imprints of Gravitational Millilensing on the Light Curve of Gamma-Ray Bursts. *ApJ*, 922(1):77.

Klypin, A., Yepes, G., Gottlöber, S., Prada, F., and Heß, S. (2016). MultiDark simulations: the story of dark matter halo concentrations and density profiles. *MNRAS*, 457(4):4340–4359.

Kulkarni, M. and Ostriker, J. P. (2022). What is the halo mass function in a fuzzy dark matter cosmology? *MNRAS*, 510(1):1425–1430.

Lapi, A., Negrello, M., González-Nuevo, J., Cai, Z. Y., De Zotti, G., and Danese, L. (2012). Effective Models for Statistical Studies of Galaxy-scale Gravitational Lensing. *ApJ*, 755(1):46.

Lazar, A., Bullock, J. S., Boylan-Kolchin, M., Moustakas, L., and Nierenberg, A. (2023). An analytic surface density profile for ΛCDM halos and gravitational lensing studies. *arXiv e-prints*, page arXiv:2304.11177.

Leung, C., Kader, Z., Masui, K. W., Dobbs, M., Michilli, D., Mena-Parra, J., Mckinven, R., Ng, C., Bandura, K., Bhardwaj, M., Brar, C., Cassanelli, T., Chawla, P., Dong, F. A., Good, D., Kaspi, V., Lanman, A. E., Lin, H.-H., Meyers, B. W., Pearlman, A. B., Pen, U.-L., Petroff, E., Pleunis, Z., Rafiei-Ravandi, M., Rahman, M., Sanghavi, P., Scholz, P.,

Shin, K., Siegel, S., Smith, K. M., Stairs, I., Tendulkar, S. P., and Vanderlinde, K. (2022). Constraining primordial black holes using fast radio burst gravitational-lens interferometry with CHIME/FRB. *Phys. Rev. D*, 106(4):043017.

Lovell, M. R. (2020a). The halo mass function in alternative dark matter models. *MNRAS*, 493(1):L11–L15.

Lovell, M. R. (2020b). Toward a General Parameterization of the Warm Dark Matter Halo Mass Function. *ApJ*, 897(2):147.

Lovell, M. R., Eke, V., Frenk, C. S., Gao, L., Jenkins, A., Theuns, T., Wang, J., White, S. D. M., Boyarsky, A., and Ruchayskiy, O. (2012). The haloes of bright satellite galaxies in a warm dark matter universe. *MNRAS*, 420(3):2318–2324.

Lovell, M. R., Frenk, C. S., Eke, V. R., Jenkins, A., Gao, L., and Theuns, T. (2014). The properties of warm dark matter haloes. *MNRAS*, 439(1):300–317.

Malkin, Z. (2018). A New Version of the OCARS Catalog of Optical Characteristics of Astrometric Radio Sources. *ApJS*, 239(2):20.

Melott, A. L. and Schramm, D. N. (1985). Can 'warm' particles provide the missing mass in dwarf galaxies? *ApJ*, 298:1–7.

Meneghetti, M., Davoli, G., Bergamini, P., Rosati, P., Natarajan, P., Giocoli, C., Caminha, G. B., Metcalf, R. B., Rasia, E., Borgani, S., Calura, F., Grillo, C., Mercurio, A., and Vanzella, E. (2020). An excess of small-scale gravitational lenses observed in galaxy clusters. *Science*, 369(6509):1347–1351.

Merritt, D., Graham, A. W., Moore, B., Diemand, J., and Terzić, B. (2006). Empirical Models for Dark Matter Halos. I. Nonparametric Construction of Density Profiles and Comparison with Parametric Models. *AJ*, 132(6):2685–2700.

Mo, H., van den Bosch, F. C., and White, S. (2010). *Galaxy Formation and Evolution*. Cambridge University Press.

Myers, S. T., Jackson, N. J., Browne, I. W. A., de Bruyn, A. G., Pearson, T. J., Readhead, A. C. S., Wilkinson, P. N., Biggs, A. D., Blandford, R. D., Fassnacht, C. D., Koopmans, L. V. E., Marlow, D. R., McKean, J. P., Norbury, M. A., Phillips, P. M., Rusin, D., Shepherd, M. C., and Sykes, C. M. (2003). The Cosmic Lens All-Sky Survey - I. Source selection and observations. *MNRAS*, 341(1):1–12.

Naderi, T., Malekjani, M., and Pace, F. (2015). Evolution of spherical overdensities in holographic dark energy models. *MNRAS*, 447(2):1873–1884.

Navarro, J. F., Frenk, C. S., and White, S. D. M. (1995). Simulations of X-ray clusters. *MNRAS*, 275(3):720–740.

Navarro, J. F., Frenk, C. S., and White, S. D. M. (1996). The Structure of Cold Dark Matter Halos. *ApJ*, 462:563.

Navarro, J. F., Frenk, C. S., and White, S. D. M. (1997). A Universal Density Profile from Hierarchical Clustering. *ApJ*, 490(2):493–508.

Navarro, J. F., Hayashi, E., Power, C., Jenkins, A. R., Frenk, C. S., White, S. D. M., Springel, V., Stadel, J., and Quinn, T. R. (2004). The inner structure of ΛCDM haloes - III. Universality and asymptotic slopes. *MNRAS*, 349(3):1039–1051.

Neto, A. F., Gao, L., Bett, P., Cole, S., Navarro, J. F., Frenk, C. S., White, S. D. M., Springel, V., and Jenkins, A. (2007). The statistics of Λ CDM halo concentrations. *MNRAS*, 381(4):1450–1462.

Page, L., Nolta, M. R., Barnes, C., Bennett, C. L., Halpern, M., Hinshaw, G., Jarosik, N., Kogut, A., Limon, M., Meyer, S. S., Peiris, H. V., Spergel, D. N., Tucker, G. S., Wollack, E., and Wright, E. L. (2003). First-Year Wilkinson Microwave Anisotropy Probe (WMAP) Observations: Interpretation of the TT and TE Angular Power Spectrum Peaks. *ApJS*, 148(1):233–241.

Pavlidou, V. and Fields, B. D. (2005). Double distribution of dark matter halos with respect to mass and local overdensity. *Phys. Rev. D*, 71(4):043510.

Perivolaropoulos, L. and Skara, F. (2022). Challenges for ΛCDM: An update. *New A Rev.*, 95:101659.

Perlmutter, S., Aldering, G., Goldhaber, G., Knop, R. A., Nugent, P., Castro, P. G., Deustua, S., Fabbro, S., Goobar, A., Groom, D. E., Hook, I. M., Kim, A. G., Kim, M. Y., Lee, J. C., Nunes, N. J., Pain, R., Pennypacker, C. R., Quimby, R., Lidman, C., Ellis, R. S., Irwin, M., McMahon, R. G., Ruiz-Lapuente, P., Walton, N., Schaefer, B., Boyle, B. J., Filippenko, A. V., Matheson, T., Fruchter, A. S., Panagia, N., Newberg, H. J. M., Couch, W. J., and Project, T. S. C. (1999). Measurements of Ω and Λ from 42 High-Redshift Supernovae. *ApJ*, 517(2):565–586.

Prada, F., Klypin, A. A., Cuesta, A. J., Betancort-Rijo, J. E., and Primack, J. (2012). Halo concentrations in the standard Λ cold dark matter cosmology. *MNRAS*, 423(4):3018–3030.

Press, W. H. and Gunn, J. E. (1973). Method for Detecting a Cosmological Density of Condensed Objects. *ApJ*, 185:397–412.

Press, W. H. and Schechter, P. (1974). Formation of Galaxies and Clusters of Galaxies by Self-Similar Gravitational Condensation. *ApJ*, 187:425–438.

Ragagnin, A., Dolag, K., Moscardini, L., Biviano, A., and D'Onofrio, M. (2019). Dependency of halo concentration on mass, redshift and fossilness in Magneticum hydrodynamic simulations. *MNRAS*, 486(3):4001–4012.

Ragagnin, A., Saro, A., Singh, P., and Dolag, K. (2021). Cosmology dependence of halo masses and concentrations in hydrodynamic simulations. *MNRAS*, 500(4):5056–5071.

Retana-Montenegro, E., van Hese, E., Gentile, G., Baes, M., and Frutos-Alfaro, F. (2012). Analytical properties of Einasto dark matter haloes. *A&A*, 540:A70.

Rocha, M., Peter, A. H. G., Bullock, J. S., Kaplinghat, M., Garrison-Kimmel, S., Oñorbe, J., and Moustakas, L. A. (2013). Cosmological simulations with self-interacting dark matter - I. Constant-density cores and substructure. *MNRAS*, 430(1):81–104.

Rubin, V. C., Ford, W. K., J., and Thonnard, N. (1980). Rotational properties of 21 SC galaxies with a large range of luminosities and radii, from NGC 4605 (R=4kpc) to UGC 2885 (R=122kpc). *ApJ*, 238:471–487.

Sbarrato, T., Ghisellini, G., Tagliaferri, G., Tavecchio, F., Ghirlanda, G., and Costamante, L. (2022). Blazar nature of high-z radio-loud quasars. *A&A*, 663:A147.

Schneider, A., Smith, R. E., Macciò, A. V., and Moore, B. (2012). Non-linear evolution of cosmological structures in warm dark matter models. *MNRAS*, 424(1):684–698.

Schwabe, B., Niemeyer, J. C., and Engels, J. F. (2016). Simulations of solitonic core mergers in ultralight axion dark matter cosmologies. *Phys. Rev. D*, 94(4):043513.

Seppi, R., Comparat, J., Nandra, K., Bulbul, E., Prada, F., Klypin, A., Merloni, A., Predehl, P., and Ider Chitham, J. (2021). The mass function dependence on the dynamical state of dark matter haloes. *A&A*, 652:A155.

Shan, H., Kneib, J.-P., Li, R., Comparat, J., Erben, T., Makler, M., Moraes, B., Van Waerbeke, L., Taylor, J. E., Charbonnier, A., and Pereira, M. E. S. (2017). The Mass-Concentration Relation and the Stellar-to-halo Mass Ratio in the CFHT Stripe 82 Survey. *ApJ*, 840(2):104.

Sheth, R. K., Mo, H. J., and Tormen, G. (2001). Ellipsoidal collapse and an improved model for the number and spatial distribution of dark matter haloes. *MNRAS*, 323(1):1–12.

Spergel, D. N. and Steinhardt, P. J. (2000). Observational Evidence for Self-Interacting Cold Dark Matter. *Phys. Rev. Lett.*, 84(17):3760–3763.

Tinker, J., Kravtsov, A. V., Klypin, A., Abazajian, K., Warren, M., Yepes, G., Gottlöber, S., and Holz, D. E. (2008). Toward a Halo Mass Function for Precision Cosmology: The Limits of Universality. *ApJ*, 688(2):709–728.

Tulin, S. and Yu, H.-B. (2018). Dark matter self-interactions and small scale structure. *Phys. Rep.*, 730:1–57.

Vegetti, S., Lagattuta, D. J., McKean, J. P., Auger, M. W., Fassnacht, C. D., and Koopmans, L. V. E. (2012). Gravitational detection of a low-mass dark satellite galaxy at cosmological distance. *Nature*, 481(7381):341–343.

Viel, M., Lesgourgues, J., Haehnelt, M. G., Matarrese, S., and Riotto, A. (2005). Constraining warm dark matter candidates including sterile neutrinos and light gravitinos with WMAP and the Lyman-α forest. *Phys. Rev. D*, 71(6):063534.

Wang, J., Bose, S., Frenk, C. S., Gao, L., Jenkins, A., Springel, V., and White, S. D. M. (2020). Universal structure of dark matter haloes over a mass range of 20 orders of magnitude. *Nature*, 585(7823):39–42.

Weinberg, S. (1972). *Gravitation and Cosmology: Principles and Applications of the General Theory of Relativity*. Wiley, New York, NY.

White, M. (2001). The mass of a halo. *A&A*, 367:27–32.

Wilkinson, P. N., Henstock, D. R., Browne, I. W., Polatidis, A. G., Augusto, P., Readhead, A. C., Pearson, T. J., Xu, W., Taylor, G. B., and Vermeulen, R. C. (2001). Limits on the Cosmological Abundance of Supermassive Compact Objects from a Search for Multiple Imaging in Compact Radio Sources. *Phys. Rev. Lett.*, 86(4):584–587.

Wright, C. O. and Brainerd, T. G. (2000). Gravitational Lensing by NFW Halos. *ApJ*, 534(1):34–40.

Yang, D. and Yu, H.-B. (2021). Self-interacting dark matter and small-scale gravitational lenses in galaxy clusters. *Phys. Rev. D*, 104(10):103031.

Yang, D. and Yu, H.-B. (2022). Gravothermal evolution of dark matter halos with differential elastic scattering. *arXiv e-prints*, page arXiv:2205.03392.

Zackrisson, E. and Riehm, T. (2007). High-redshift microlensing and the spatial distribution of dark matter in the form of MACHOs. *A&A*, 475(2):453–465.

Zackrisson, E. and Riehm, T. (2010). Gravitational Lensing as a Probe of Cold Dark Matter Subhalos. *Advances in Astronomy*, 2010:478910.

Zavala, J. and Frenk, C. S. (2019). Dark Matter Haloes and Subhaloes. *Galaxies*, 7(4):81.

Zavala, J., Vogelsberger, M., and Walker, M. G. (2013). Constraining self-interacting dark matter with the Milky way's dwarf spheroidals. *MNRAS*, 431:L20–L24.

Zhou, H., Li, Z., Huang, Z., Gao, H., and Huang, L. (2022a). Constraints on the abundance of primordial black holes with different mass distributions from lensing of fast radio bursts. *MNRAS*, 511(1):1141–1152.

Zhou, H., Li, Z., Liao, K., Niu, C., Gao, H., Huang, Z., Huang, L., and Zhang, B. (2022b). Search for Lensing Signatures from the Latest Fast Radio Burst Observations and Constraints on the Abundance of Primordial Black Holes. *ApJ*, 928(2):124.

Zhou, H., Lian, Y., Li, Z., Cao, S., and Huang, Z. (2022c). Constraints on the abundance of supermassive primordial black holes from lensing of compact radio sources. *MNRAS*, 513(3):3627–3633.

Zwicky, F. (1933). Die Rotverschiebung von extragalaktischen Nebeln. *Helvetica Physica Acta*, 6:110–127.

Appendix A

Press-Schechter mass function

In this appendix, we offer a short prescription for calculating the halo mass function. For more details on the subject, see Mo et al. (2010).

A.1 Preliminaries

Suppose that matter was initially uniformly distributed in space (Universe) with a mean matter density ρ_m. Due to quantum mechanical effects, small local fluctuations appeared in the mass density $\rho(\vec{x})$. It is convenient to define the density field $\delta(\vec{x})$, which quantifies the fractional deviation of the mass-density at $\vec{x}$ from the mean matter density. The density field is given by

$$\delta(\vec{x}) = \frac{\rho(\vec{x}) - \rho_m}{\rho_m}, \tag{A.1}$$

and as we will see below, this density field can be well described by the initial power spectrum $P_{init}(k)$.

Obviously, these fluctuations evolved in time, since matter experiences gravity the Universe is not static but expands. As a result, the density field is time dependent and varies through time. According to the linear theory we can write down the following equation

$$\delta(\vec{x},t) = D(t)\delta_0(\vec{x}), \tag{A.2}$$

where $D(t)$ is the linear growth normalized to $D(t_o) = 1$ and $\delta_0(\vec{x})$ denotes the density field linearly extrapolated to $t = t_o$. We remark that, the $D(t)$ is strongly dependent on the cosmology. The mean density field is given by

$$\langle\delta\rangle = \frac{1}{V}\int_{\mathscr{V}} \delta(\vec{x})d^3\vec{x}, \tag{A.3}$$

while the variance in the density field is calculated by

$$\sigma^2 = \langle \delta(\vec{x})\delta(\vec{x})\rangle = \frac{1}{V}\int_{\mathscr{V}} \delta^2(\vec{x})d^3\vec{x}, \tag{A.4}$$

and the correlation function is defined as

$$\begin{aligned}\xi(\vec{r}) &= \langle \delta(\vec{x})\delta(\vec{x}+\vec{r})\rangle \\ &= \frac{1}{(2\pi)^6}\left\langle \int \delta(\vec{k})e^{i\vec{k}\cdot(\vec{x}+\vec{r})}d^3\vec{k}\int \delta(\vec{k}')e^{i\vec{k}'\cdot\vec{x}}d^3\vec{k}'\right\rangle.\end{aligned} \tag{A.5}$$

Now, if we write the $\delta(\vec{k})$ in the following form

$$\delta(\vec{k}) = |\delta_k|e^{i\phi_k}, \tag{A.6}$$

then it yields

$$\begin{aligned}\xi(\vec{r}) &= \frac{1}{V}\int \frac{d^3\vec{k}}{(2\pi)^3}\,|\delta_k|^2\,e^{i\vec{k}\cdot\vec{r}} \\ &= \frac{1}{(2\pi)^3}\int P(k)e^{i\vec{k}\cdot\vec{r}}d^3\vec{k},\end{aligned} \tag{A.7}$$

where $P(k)$ is the matter power spectrum and is given by

$$P(k) = \frac{1}{V}\,|\delta_k|^2. \tag{A.8}$$

Obviously, if we set $\vec{r} = 0$ in the correlation function we end up with the variance σ^2, which usually is written in the following form

$$\sigma^2 = \int_{k=0}^{k=\infty} \Delta^2(k)\frac{dk}{k}, \tag{A.9}$$

where

$$\Delta^2(k) = \frac{k^3P(k)}{2\pi^2},$$

is the unit-less power spectrum.

Smoothing

In order to proceed to the derivation of the Press-Schechter mass function, it is convenient to introduce a useful technique, called smoothing method, which has been extensively discussed

and adopted in the related literature extensively. According to this technique, we have to smooth out the density field and therefore the variance by using a window function $W(\vec{x};R)$ (called "filter") that is normalized such that

$$\int_{\mathscr{V}} W(\vec{x};R)d^3\vec{x} = 1, \tag{A.10}$$

where R is the characteristic (scale) radius of the "filter" and dictates the smoothing. The smoothed density field is given by

$$\delta(\vec{x};R) = \int_{\mathscr{V}} \delta(\vec{x}')W(\vec{x}-\vec{x}';R)d^3\vec{x}'. \tag{A.11}$$

Note that, instead of using the a characteristic length scale, we can equivalently define a characteristic mass M that is related to the radius R through

$$M = \gamma_f \rho_m R^3, \tag{A.12}$$

where the γ_f parameter depends on the shape of the "filter" and is calculated by the following expression (Mo et al., 2010)

$$\gamma_f^{-1} = R^3 W(0;R). \tag{A.13}$$

The Fourier transform of the smoothed density field is

$$\begin{aligned}\delta(\vec{k};R) &= \int \delta(\vec{x};R)e^{-i\vec{k}\cdot\vec{x}}d^3\vec{x} \\ &= \int d^3\vec{x}'\,\delta(\vec{x}')e^{-i\vec{k}\cdot\vec{x}'}\int d^3\vec{x}W(\vec{x}-\vec{x}';R)e^{-i\vec{k}\cdot(\vec{x}-\vec{x}')} \\ &= \delta(k)W(\vec{k};R),\end{aligned} \tag{A.14}$$

where we employed Eq. (A.11). $W(\vec{k},R)$ is the "filter" function in the Fourier space (k-space)

$$W(\vec{k};R) = \int W(\vec{x};R)e^{-i\vec{k}\cdot\vec{x}}d^3\vec{x}. \tag{A.15}$$

The variance of the smoothed density field is given by

$$\sigma^2 = \left\langle \delta^2(\vec{x};R)\right\rangle = \frac{1}{2\pi^2}\int_0^\infty P(k)W^2(kR)k^2dk, \tag{A.16}$$

where we considered that $W(\vec{k},R)$ depends only on the variable $|\vec{k}|R$ (e.g., Eq. A.29; see also Mo et al. 2010).

A.2 Press Schechter formalism

Assume the density field $\delta(\vec{x})$ to be a Gaussian random field, then so is the $\delta(\vec{x};R)$. Thus, we can write the following general formula that describes a Gaussian distribution of the density field

$$P(\delta_M)d\delta_M = \frac{1}{\sqrt{2\pi\sigma_M^2}} \exp\left(-\frac{\delta_M^2}{2\sigma_M^2}\right) d\delta_M, \tag{A.17}$$

where $\delta_M = \delta(\vec{x};R)$ and $\sigma_M = \sigma(M) = \sigma(R)$.

Supposing the model describing the formation of the haloes is the spherical collapse model, then regions with $\delta_M > \delta_c(t)$ will collapse to form dark matter haloes. The $\delta_c(t)$ quantity is called critical overdensity, which turns out to be equal to $\delta_c(0)/D(t)$ (see, Eq. C30 in Pavlidou and Fields, 2005) and is the minimum overdensity required for a region to collapse into forming a halo.

Press-Schechter postulate (Press and Schechter, 1974): The probability that $\delta_M > \delta_c(t)$ is equal to the mass fraction that at time t is contained in haloes with mass greater than M. Mathematically, it is translated to

$$\begin{aligned} F(>M,t) &= \mathscr{P}_{>\delta_c} = \int_{\delta_c}^{\infty} P(\delta_M)d\delta_M \\ \implies F(>M,t) &= \frac{1}{2}\,\mathrm{erfc}\left[\frac{\delta_c(t)}{2\sigma_M}\right], \end{aligned} \tag{A.18}$$

but, in the limit $M \to 0$, the variance becomes $\lim_{M\to 0}\sigma_M \to \infty$, which yields $F(>0,t) = \mathrm{erfc}(0) = 1/2$. Nevertheless, the mass fraction $F(>M,t)$ must tend to 1 as $M \to 0$, so a fudge factor equals 2 must be inserted manually in Eq. (A.18), in order to give us a correct result. Therefore, we deduce

$$F(>M,t) = 2\mathscr{P}_{>\delta_c}. \tag{A.19}$$

A.3 Deriving the differential halo mass function

The differential halo mass function, which represents the number density of collapsed haloes with mass in the range $[M, M+\mathrm{d}M]$, is defined as

$$n(M,t) = \frac{dN}{dM} = \frac{1}{M}\frac{dN}{d\ln M}. \tag{A.20}$$

Using the Press-Schechter (PS) postulate and Eq. (A.19), we can obtain a formula for dN/dM as follows. Subtracting the $F(M+dM)$ fraction from the $F(>M)$, we get the fraction of mass that is locked up in haloes with masses in the range $[M, M+\mathrm{d}M]$. So, if we multiply it with the mean matter density and divide by M, we end up with the following expression that corresponds to the differential halo mass function:

$$\frac{dN}{dM} = \frac{\rho_m}{M}\frac{\partial}{\partial M}F(>M,t). \tag{A.21}$$

Substituting Eqs. (A.18), (A.19) into Eq. (A.21), we finally obtain

$$\begin{aligned} n(M) &= 2\frac{\rho_m}{M}\frac{\partial}{\partial M}\mathscr{P}_{>\delta_c} \\ &= 4\frac{\rho_m}{\sqrt{2\pi}M}\frac{\partial}{\partial M}\int_{\delta_c/2\sigma_M}^{\infty} du e^{-u^2} \\ &= -\sqrt{2/\pi}\frac{\rho_m}{M}\frac{\delta_c}{\sigma_M^2}\frac{d\sigma_M}{dM}\exp(-\delta_c^2/2\sigma_M^2) \\ &= \sqrt{2/\pi}\frac{\rho_m}{M}\frac{\delta_c}{\sigma_M^2}\left|\frac{d\sigma_M}{dM}\right|\exp(-\delta_c^2/2\sigma_M^2). \end{aligned} \tag{A.22}$$

A.4 Halo mass function

Using the Press-Schechter formalism, we found the differential halo mass function to be (Press and Schechter, 1974)

$$n(M,z) \equiv \frac{dN}{dM} = \sqrt{\frac{2}{\pi}}\frac{\rho_m(z)}{M}\frac{\delta_c(z)}{\sigma_M^2}\left|\frac{d\sigma_M}{dM}\right|\exp\left[-\frac{\delta_c^2(z)}{2\sigma_M^2}\right], \tag{A.23}$$

where $\rho_m(z) = \Omega_m(1+z)^3$, $\delta_c(z)$ is the overdensity of a structure collapsing at redshift z linearly extrapolated to the present epoch, and σ_M accounts for the linear rms fluctuation (variance) of the density field on scale M. Under the spherical collapse assumption and concordance cosmology, the critical overdensity is given by (e.g., Eq. C30 in Pavlidou and Fields, 2005)

$$\delta_c(z) = \frac{1}{D(z)}\delta_c(0), \tag{A.24}$$

where $D(z)$ is the normalized linear growth factor, that is $D(z=0)=1$, calculated by

$$D(z) = G\left[(2\omega)^{1/3}/(1+z)\right]/G\left[(2\omega)^{1/3}\right], \tag{A.25}$$

while $\omega = \Omega_\Lambda/\Omega_m$ and

$$G(u) = \frac{(2+u^3)^{1/2}}{u^{3/2}} \int_0^u \frac{y^{3/2}}{(2+y^3)^{3/2}} dy. \tag{A.26}$$

The variance σ_M, normalized to be equal to σ_8 when $R = 8h^{-1}$ Mpc, is given by (see Eq. 10 in Pavlidou and Fields, 2005)

$$\sigma_M^2 = \sigma_8^2 \frac{\int_0^\infty dk\, P(k) W^2(kR(M)) k^2}{\int_0^\infty dk\, P(k) W^2(k8h^{-1}\,\mathrm{Mpc}) k^2}, \tag{A.27}$$

where the σ_8 parameter is a direct observable quantity, while $W(kR)$ refers to the window function (filter) and R is the characteristic radius of the filter related to the mass M through

$$R(M) = \left(\frac{M}{\gamma_f \rho_m}\right)^{1/3}, \tag{A.28}$$

where γ_f is a parameter depending on the shape of the filter. Here, we employ a sharp in k-space filter given by

$$W(\vec{k};R) = \begin{cases} 1 & \text{if } |\vec{k}| \leq R^{-1} \\ 0 & \text{if } |\vec{k}| > R^{-1} \end{cases}. \tag{A.29}$$

Given this choice, γ_f becomes equal to $6\pi^2$ (Mo et al., 2010).

In Eq. (A.27), P(k) stands for the linear matter power spectrum. Invoking linear theory, we can write the matter power spectrum to be

$$P(k) \propto T^2(k) P_{init}(k), \tag{A.30}$$

where P_{init} is the initial power spectrum proportional to k^n with $n = 0.97$, while $T(k)$ corresponds to the transfer function. Bond and Efstathiou (1984) offer the following simple numerical formula for the transfer function $T(k)$, which is consistent with the ΛCDM model (see also Jenkins et al., 2001)

$$T(k) = \frac{1}{\left[1 + \left[aq + (bq)^{3/2} + (cq)^2\right]^\nu\right]^{1/\nu}}, \tag{A.31}$$

where $q = k/\Gamma$, $\Gamma = \Omega_{m,0}h$, $\nu = 1.13$, $a = 6.4\,h^{-1}$ Mpc, $b = 3\,h^{-1}$ Mpc, and $c = 1.7\,h^{-1}$ Mpc.